(2)

NRL Report 8797

AD-A141 921

A High-Resolution Target-Tracking Concept Using Spectral Estimation Techniques

WILLIAM F. GABRIEL

Electromagnetics Branch
Radar Division

May 31, 1984

NAVAL RESEARCH LABORATORY
Washington, D.C.

REPORT DOCUMENTATION PAGE

1a REPORT SECURITY CLASSIFICATION UNCLASSIFIED	1b RESTRICTIVE MARKINGS
2a SECURITY CLASSIFICATION AUTHORITY	3 DISTRIBUTION AVAILABILITY OF REPORT Approved for pubiic release; distribution unlimitcd.
2b DECLASSIFICATION DOWNGRADING SCHEDULE	
4 PERFORMING ORGANIZATION REPORT NUMBER(S) NRL Report 8797	5 MONITORING ORGANIZATION REPORT NUMBER(S)
6a NAME OF PERFORMING ORGANIZATION Naval Research Laboratory 6b OFFICE SYMBOL (If applicable) Code 5370	7a NAME OF MONITORING ORGANIZATION
6c ADDRESS (City, State and ZIP Code) Washington, DC 20375	7b ADDRESS (City, State and ZIP Code)
8a NAME OF FUNDING/SPONSORING ORGANIZATION (See Page ii) 8b OFFICE SYMBOL (If applicable)	9 PROCUREMENT INSTRUMENT IDENTIFICATION NUMBER
8c ADDRESS (City, State and ZIP Code) 1. Arlington, VA 22217 2. Washington, DC 20361	10 SOURCE OF FUNDING NOS PROGRAM ELEMENT NO: 61153N PROJECT NO: TASK NO: RR0210543 / WR02101000 WORK UNIT NO: DN680-369 / DN680-044
11 TITLE (Include Security Classification) (See Page ii)	
12 PERSONAL AUTHOR(S) William F. Gabriel	
13a TYPE OF REPORT Interim 13b TIME COVERED FROM TO	14 DATE OF REPORT (Yr., Mo., Day) 1984 May 31 15 PAGE COUNT 55
16 SUPPLEMENTARY NOTATION	
17 COSATI CODES FIELD / GROUP / SUB GR	18 SUBJECT TERMS (Continue on reverse if necessary and identify by block number) Adaptive arrays; Antennas; Nonlinear processing; Spectral analysis; Tracking; Digital processing; Optimal estimation; Spatial filters

19 ABSTRACT (Continue on reverse if necessary and identify by block number)

A target-tracking concept based on modern spectral estimation techniques combined with adaptive array processing has been investigated to attain 'superresolution' tracking performance. The goal is to achieve satisfactory monopulse track angle estimates in the presence of strong multiple interference sources which are located within a beamwidth of the target. This application area was addressed via an all-digital receive system concept whereby adaptive spatial filter weights are periodically updated on the basis of source estimates, and the filter output residue signals are then sifted for targets. This report includes several radar-simulation examples to illustrate some of the processing step outputs, tracking beam distortions, corrections for target wavefront distortions, and tracking in the presence of closely spaced interference sources. It also contains a section devoted to the algorithm theory, analysis, and development which will help to understand the various processing steps involved.

20 DISTRIBUTION/AVAILABILITY OF ABSTRACT UNCLASSIFIED/UNLIMITED ☒ SAME AS RPT ☐ DTIC USERS ☐	21 ABSTRACT SECURITY CLASSIFICATION UNCLASSIFIED
22a NAME OF RESPONSIBLE INDIVIDUAL William F. Gabriel	22b TELEPHONE NUMBER (Include Area Code) (202) 767-2584 22c OFFICE SYMBOL Code 5370

DD FORM 1473, 83 APR EDITION OF 1 JAN 73 IS OBSOLETE

20. ABSTRACT (Continued)

8a. NAME OF FUNDING/SPONSORING ORGANIZATION (Continued)

1. Office of Naval Research
2. Naval Air Systems Command

11. TITLE (Include Security Classification) (Continued)

A High-Resolution Target-Tracking Concept
Using Spectral Estimation Techniques

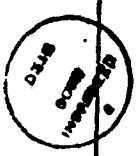

Accession For	
NTIS GRA&I	☑
DTIC TAB	☐
Unannounced	☐
Justification	
By	
Distribution/	
Availability Codes	
Dist	Avail and/or Special
A-1	

CONTENTS

A HIGH-RESOLUTION TARGET-TRACKING CONCEPT USING SPECTRAL ESTIMATION TECHNIQUES

1. INTRODUCTION

The tracking of targets in the presence of nearby strong interference sources is a problem area of considerable interest in radar systems, primarily because conventional tracking radars may experience large errors, track-breaking, or complete disruption. Some early proposed solutions to this problem evolved from the growing adaptive array antenna technology of the 1970's. For example, a paper by White [1] discusses the high-resolution aspect in considerable detail. He presents the problem of tracking radar targets in the low-angle regime where conventional tracking radars encounter difficulty because of the presence of a strong surface-reflected ray. Starting with a classical maximum-likelihood analysis of the problem of two closely spaced targets, he develops two techniques which are theoretically capable of dealing with the multipath problem. A more recent contribution in the multipath area is the work of Cantrell et al. [2], who proposed a simple, closed form solution for an array divided into three subapertures. The accuracy of their technique compares favorably with the maximum likelihood estimate which uses all of the individual elements.

The first extension of fully adaptive arrays to angle estimation in external noise fields is the contribution of Davis et al. [3], who developed an algorithm based on the outputs of adaptively distorted sum and difference beams. The adaptive beams filter (null) the external noise sources, and distortion correction is then applied in the resultant monopulse output angle estimate for a selected tracking beam direction.

In recent years, a closely related new technology which derives largely from modern spectral estimation theory has been emerging, and it appears to offer additional opportunities for achieving significant improvements in the detection/tracking of closely spaced multiple sources and targets. Interest is stimulated because of reported resolution capabilities which extend well beyond the conventional windowed Fourier transform. Gabriel [4,5] has emphasized two processing-domain performance characteristics for these techniques which apply to the tracking problem:

- "superresolution" which implies the resolution of two or more sources within the conventional beamwidth of an RF antenna aperture, and
- "absence of sidelobes" which implies the resolution of two or more sources of unequal strengths when those sources are spaced more than a beamwidth apart.

(Quotation marks are used to avoid misinterpretation of the conventional radar system definitions of resolution and sidelobes.) These characteristics are demonstrated via simulation examples for several spectral estimation algorithms including linear prediction methods, the maximum likelihood method, and eigenvalue/eigenvector analysis techniques. References 4 and 5 also address the difficult radar coherent-source problem area which involves a phase-dependent signal-to-noise ratio (SNR) penalty.

A contribution which proposes both adaptive processing and high-resolution spectral estimation is that of Chapman et al. [6], who discusses the mainbeam jamming problem. Two techniques were

Manuscript approved December 13, 1983.

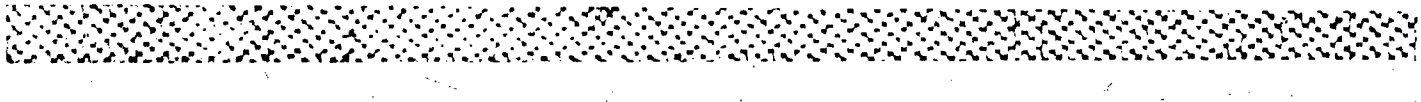

investigated. First, a linear prediction extrapolation procedure was employed to extend the apparent aperture of an antenna array and thereby achieve a narrow notch on the jammer while providing gain in the look direction of the target. Second, the maximum likelihood procedure (Section 4.4) was used to provide adaptive filtering and estimate target angle via beam scan.

The remainder of this report is divided into three principal sections. Section 2 discusses the overall tracking system concept and references the sections containing technical details, Section 3 considers several tracking performance examples which are based on computer simulation snapshot data, and Section 4 discusses the details of the associated algorithm/processing theory, analysis, and development.

2. TRACKING SYSTEM CONCEPT

An all-digital processing system is defined which commences with complex data sampling of the array element signals (or beam-port signals if it is a beamformer type of antenna). It is assumed that conventional receiver techniques would be employed prior to the signal analogue-to-digital (A/D) converters as illustrated in Fig. 1; i.e., the system may include transmit-receive (TR) devices, low-noise RF amplifiers, local oscillator (LO) mixers, intermediate frequency (IF) amplifiers, and synchronous baseband detection with in-phase and quadrature (I&Q) video output to sample and hold (S/H) circuits followed by the A/D converters. Snapshots would nominally occur at the Nyquist sampling rate corresponding to the video bandwidth, so that a radar-oriented person may view them as range bin time samplings. For this interim report, actual measured snapshot data were not used in tracking performance evaluations. Rather, a snapshot signal model described in Section 4.1 was used to generate the complex digital signal data via computer simulation.

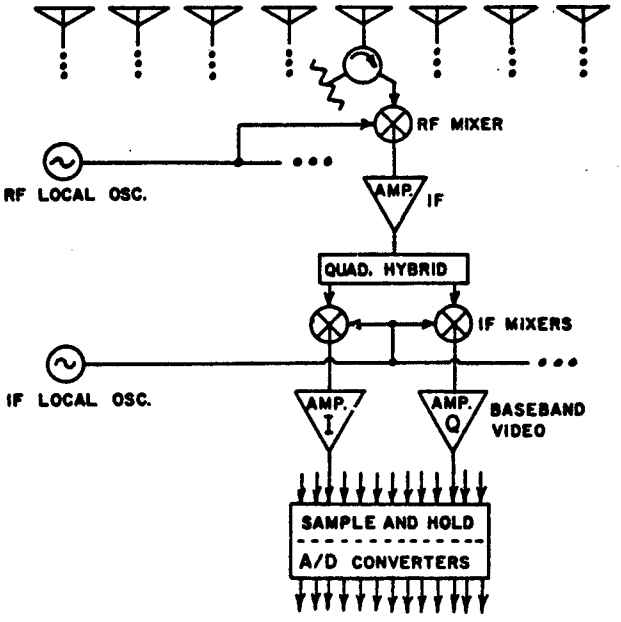

Fig. 1 — Typical RF receiver techniques associated with A/D complex-data sampling

Figure 2 shows the system concept for processing the digital signals. Starting on the left-hand side, the system continuously computes/updates a sample covariance matrix $\hat{\mathbf{R}}$. A number of techniques are available for computing $\hat{\mathbf{R}}$, and four of these are described in Section 4.2. Of particular

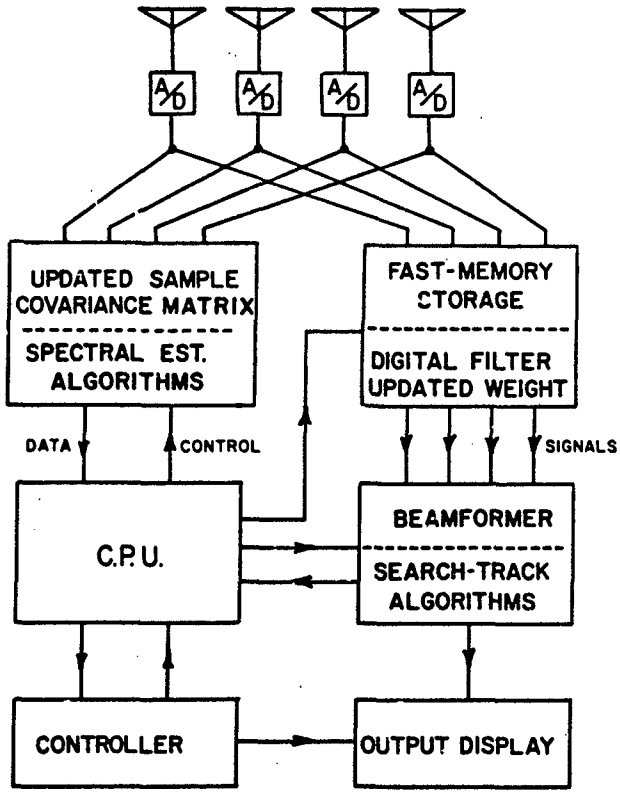

Fig. 2 — Adaptive array tracking system concept

significance is the fact that $\hat{\mathbf{R}}$ may be dimensioned either equal to or less than the number of array elements; i.e., the model order of the estimate is selectable per subaperture averaging option choice.

Off-line processing on $\hat{\mathbf{R}}$ is then conducted at periodic intervals to estimate the locations and relative power levels of interference sources via a catalogue of spectral estimation algorithms. Literally dozens of algorithms are now available in the literature, ranging from fast simple routines [4,7] for estimating strong sources, to the more sophisticated eigenanalysis routines for estimating weak sources. Because of the growing interest and superior performance of eigenvalue/eigenvector decomposition techniques, Sections 4.3 to 4.5 are devoted to a detailed discussion/analysis with pertinent references. Desirable features of any algorithm are robustness, fast root-finding, and the capability of solving for relative source strength. This latter feature is important in source classification and crucial for screening out "false alarms."

Having estimated the locations and relative power levels of interference sources, the central processor unit (CPU) then applies these data to the computation of optimized adaptive spatial filter weights. These may be developed via a number of different schemes, and Section 4.7 discusses two approaches with an option for "softened" spatial filtering. The question may be raised as to why the filter weights are not computed/developed directly from the data samples as in a conventional adaptive array. A number of reasons exist for separating source estimation from filter weight computation.

1. Source estimation often requires flexible subaperture techniques, i.e., a model order which is less than full aperture. (See Section 4.2.4.)

2. Search/track detection usually demands use of the full aperture at all times because of SNR and resolution considerations.

3. It is easier to estimate and implement prewhitening filtering to remove slowly changing interference sources and colored noise distributions.

4. It is easier to modify the filtering for purposes other than source cancellation, i.e., to reduce distortion effects or to introduce time-modulated weights.

5. One can readily add real-time adaptive filter weight perturbations to permit fast response.

6. Certain constrained, partially adaptive systems are unable to assign their degrees of freedom automatically, for example, a beamspace adaptive antenna system with a low sidelobe constraint and only a few beams available.

The right-hand side of Fig. 2 shows that the CPU also has control over a fast-memory storage capability which could be used in several different ways including

- dump-storage of a block of contiguous data snapshots; for example, one may store the snapshots associated with a particular sample covariance matrix, for later retrieval when that filter update occurs;

- time-gated snapshot storage based on interference source classification, for later selective retrieval;

- time-gated snapshot storage based on target-search considerations; and

- "bucket-brigade bumping" snapshot storage to obtain a selected time delay of the snapshots.

Thus one may select either the current snapshot or a storage snapshot for feeding into the filter weights which the CPU updates.

Next, the filtered signal output residue is fed into a beamformer which is weighted to produce the desired search and monopulse track beams for target detection/tracking. Section 4.8 discusses the unavoidable problem of target wavefront distortion which can cause serious tracking errors if not dealt with and points out two distortion correction procedures.

Recognize that Fig. 2 is intended to represent a concept rather than a specific system design. Any particular system design application would undoubtedly require variants to achieve the most efficient processor implementation. The concept is summarized in the following five steps:

1. Convert A/D at elements/beam ports.

2. Compute/update sample covariance matrix $\hat{\mathbf{K}}$.

   - model order selectable (need not be known)

   - subaperture technique incorporated

3. Process $\hat{\mathbf{R}}$ off-line periodically

   - by using fast inverse routines to estimate strong sources,

- by using eigenanalysis routines to estimate weak sources,
- by rootfinding on optimum weights to pick out source locations;
- then compute source power matrix;
- then screen false alarms.

4. Compute filter weights for full aperture from updated source information.
5. Apply conventional tracking to the filtered snapshots, incorporating wavefront distortion correction.

3. TRACK PERFORMANCE EXAMPLES

To demonstrate the concept, a series of simple radar-simulation examples are given in this section wherein a single target appears in a single range bin per pulse repetition frequency (PRF) period, and one to several interference sources appear in N adjacent range bins per PRF period. All snapshots were simulated from the model described in Section 4.1, by using an 8-element linear array with half-wavelength spacing as the receive aperture. The examples are identified as follows:

Case C8L6JVCϕB - six sources,

Case C8L1JXX - one source,

Case C8L2J3C - two sources,

Case C8L3J3C - three sources, and

Case C8L3J7B - three sources plus spatial noise.

3.1 Case C8L6JVCϕB - Six Sources

This case was originally designed in January 1981 for an 8-element array for the purpose of stressing spectral estimation algorithms. Figure 3 illustrates its range-azimuth geometry, which consists of a

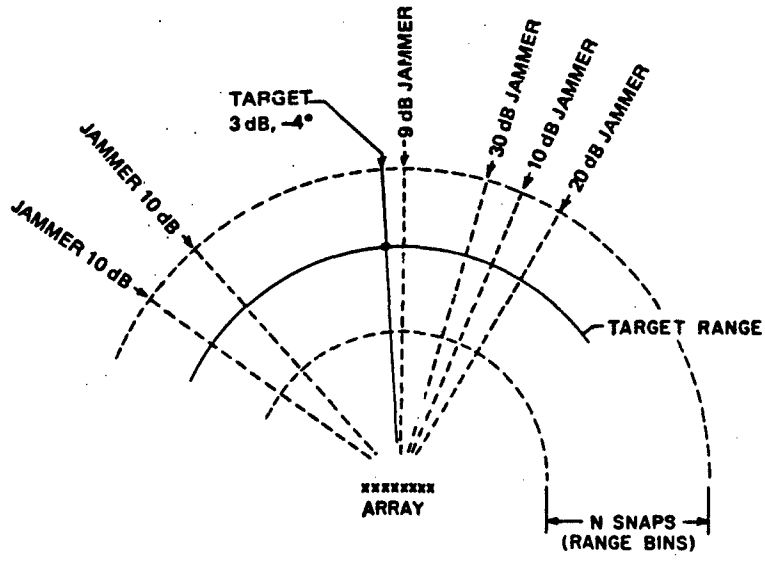

Fig. 3 — Range/azimuth geometry for Case C8L6JVCϕB

single 3 dB SNR target located at -4° azimuth and appearing in a single range bin per PRF period. Six interference sources appear in N adjacent range bins per PRF period. Two of these sources are 10 dB SNR, 95% correlated, located at −54° and −42° (0.57 beamwidth apart); and four are noncoherent sources of −9, 30, 10, and 20 dB SNR, located at 0°, 15°, 22°, and 30° respectively. The correlated sources, the close spacings, the large dynamic range of source strengths, and the consumption of six out of seven degrees of freedom causes difficulty for most spectral estimation algorithms, as shown in Fig. 4. Note in Fig. 4(a) that the conventional beam scan (windowed Fourier transform) is hopeless, as expected, because of its beamwidth and sidelobe limitations. But also note that the SLC (sidelobe canceller algorithm similar to least-squares linear prediction) has failed to resolve the highly correlated sources and the two weaker noncoherent sources located at 0° and 22°. In Fig. 4(b) the maximum likelihood method (MLM) algorithm also performs poorly, but the multiple signal classification (MUSIC) algorithm (Section 4.4.2) was able to locate all six sources correctly via its noise eigenvectors. The point to be made is that this is not an easy case to resolve.

This first case will be presented in greater walk-through detail than the others to familiarize the reader with the sequence. Starting with the computation of $\hat{\mathbf{R}}$, the simple block averaging method (Section 4.2.1) was used with $N = 256$ snapshots. Further, the filter weight update period was selected to coincide, so that a new copy of $\hat{\mathbf{R}}$ was fetched for processing at the end of each 256 snapshots period. Two spectral estimation algorithms were applied to $\hat{\mathbf{R}}$: the SLC algorithm and the principal eigenvector Gram-Schmidt (PEGS) algorithm (Section 4.4.3). The SLC algorithm develops the Wiener optimum weight [4,5], per Eq. (25) in Section 4.4.1, $\mathbf{W}_o = \mu\hat{\mathbf{R}}^{-1}\mathbf{S}^*$, where $\mathbf{S}^{*t} = [0, 0, 0, \ldots, 1]$. Rootfinding (Section 4.6) on the first four updates of $\mathbf{W}_o$ results in the Z-plane roots plots shown in fig. 5(a). Note that only three roots are close to the unit circle and would be culled, leading then to the corresponding digital power/location estimates shown in Fig. 5(b). Performance comments here are the same as those associated with Fig. 4(a); i.e., the SLC algorithm has failed to resolve the highly correlated sources and the two weaker noncoherent sources located at 0° and 22°.

The PEGS eigenanalysis algorithm applied to the same four $\hat{\mathbf{R}}$ update trials results in the roots and digital power/location estimates shown in Fig. 6. Note that the estimates are now reasonably close to the truth given in Fig. 3, with the greatest variance exhibited by the highly correlated sources and the weak −9 dB source.

After the source data are estimated, the adaptive spatial filter weights are updated accordingly (Section 4.7), and we can then compute the associated spatial filter insertion loss. Figure 7 illustrates the results for the four trials in this example, computed from Eq. (50) for $\alpha = 1$. Insertion loss plots are very helpful for visualizing certain target/interference-source relationships.

- Detection/tracking is most favorable in those regions where the insertion loss is low.
- Insertion loss cost against a desired target increases rapidly as the target gets close to a strong interference source.
- If the target strength is sufficient to overcome the insertion loss, then tracking within a beamwidth of a strong interference source should be feasible.
- Insertion loss and tracking beam distortion are related.

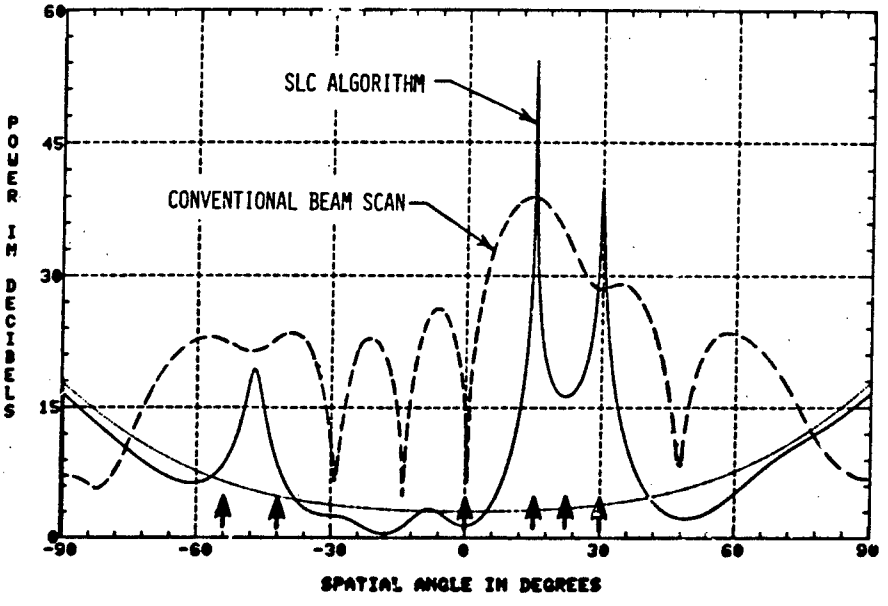

(a) Conventional/SLC algorithm

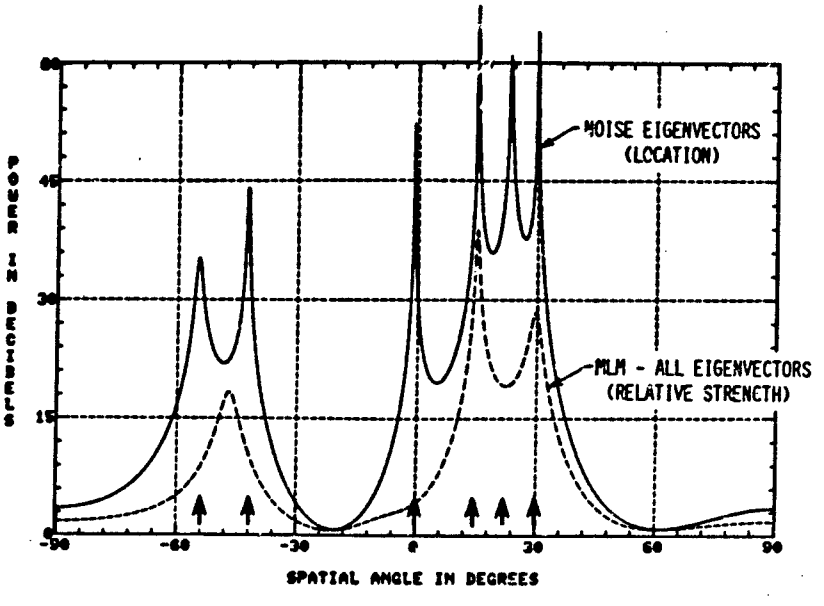

(b) MLM/eigenvector algorithm, symmetric matrix constraint

Fig. 4 — Spatial spectrum estimate for six sources: two 10 dB sources 95% correlated at −54° and −42° (0.57 beamwidth apart); four noncoherent sources of −9, 30, 10, and 20 dB strengths located at 0°, 15°, 22°, and 30°; 8-element linear array, sample covariance matrix of 1024 snapshots

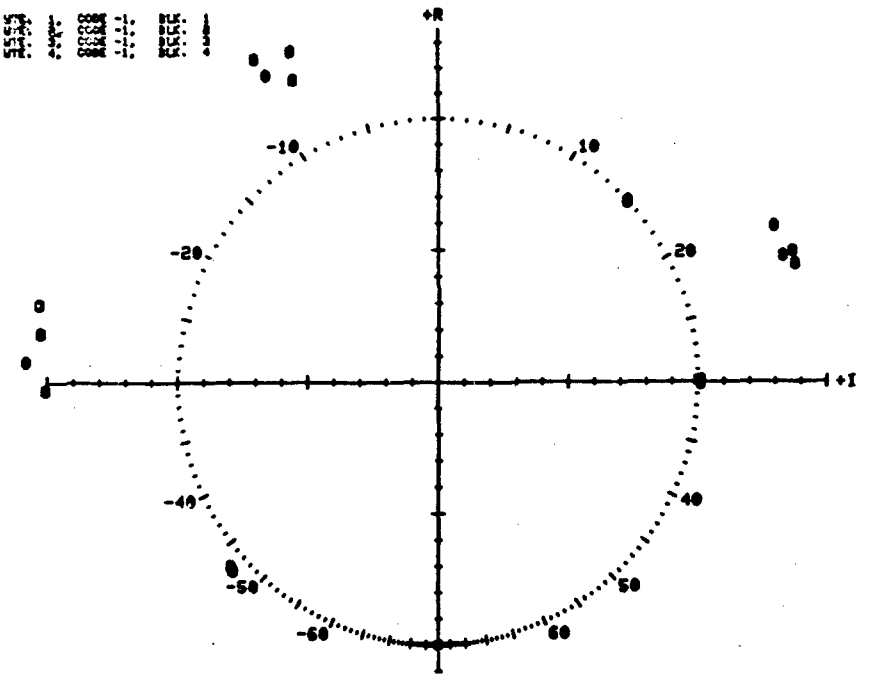

(a) Z-plane roots

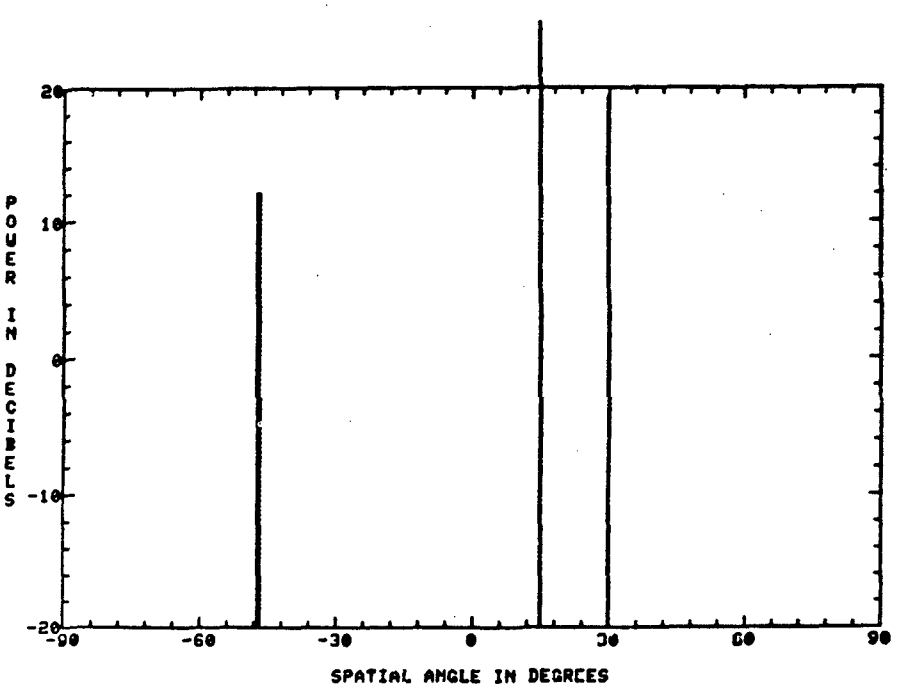

(b) Digital relative power vs location angle

Fig. 5 — Spatial spectrum estimates for Case C8L6JVCϕB, derived from SLC algorithm optimum weights, four trials of 256 snapshots

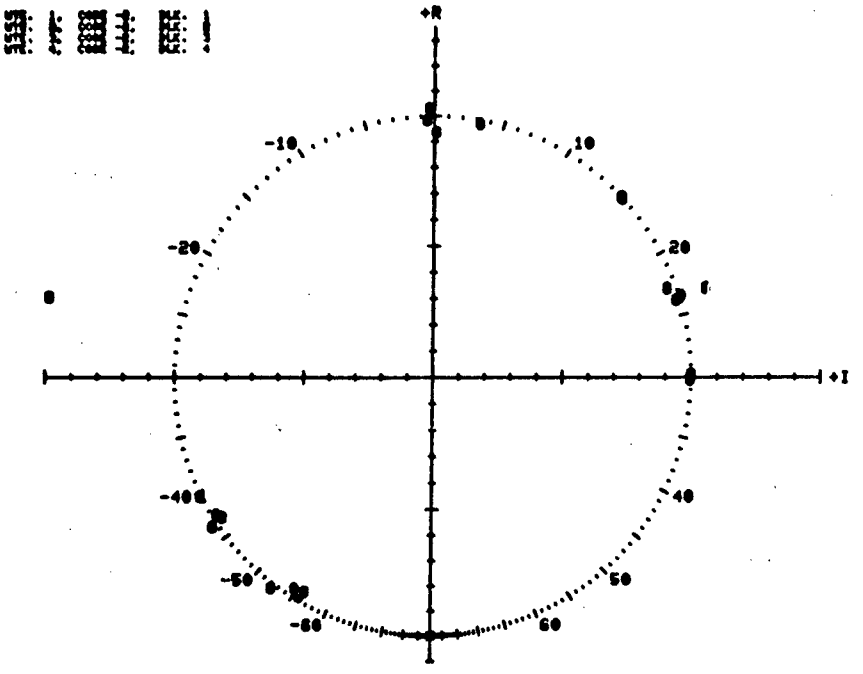

(a) Z-plane roots

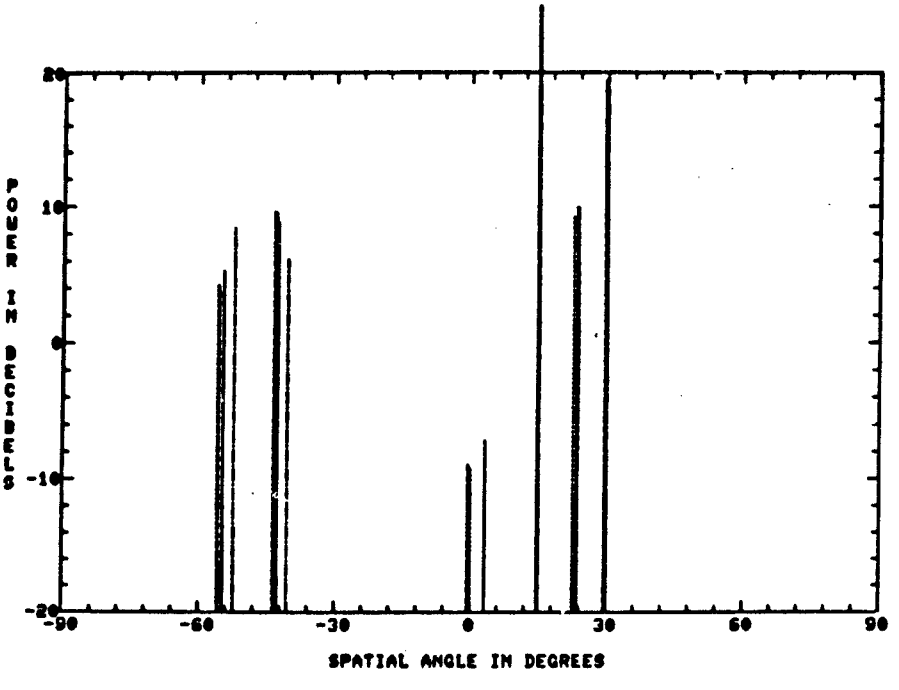

(b) Digital relative power vs location angle

Fig. 6 — Spatial spectrum estimates for Case C8L6JVCϕB, derived from PEGS eigenanalysis algorithm optimum weights, four trials of 256 snapshots

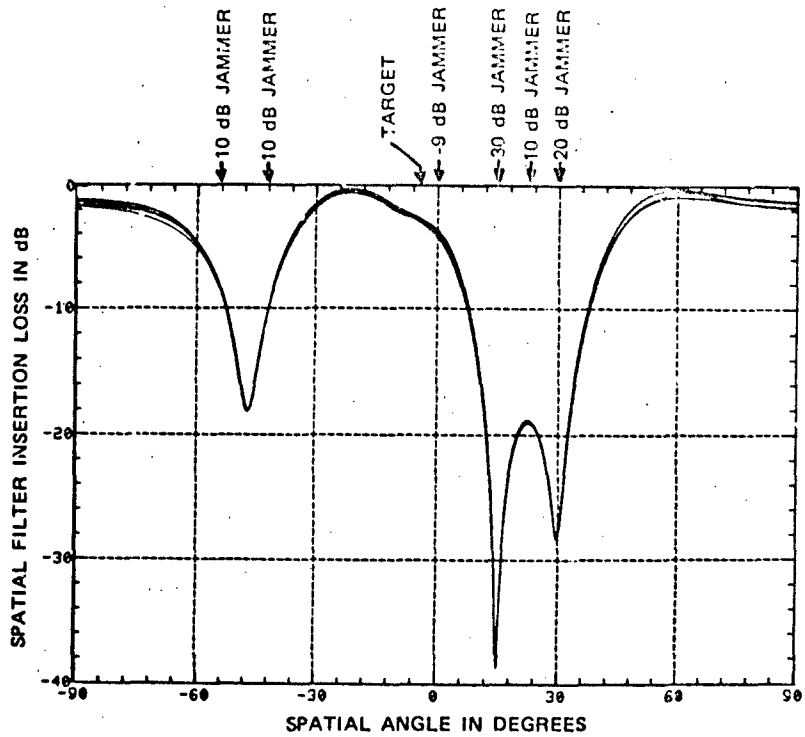

Fig. 7 — Adaptive spatial filter insertion loss

Section 4.8 discusses the formation of the tracking beams and their resultant equivalent distortion due to the spatial filtering. Figure 8 summarizes the particular distortions associated with this case; these distortions are computed for tracking beams with a boresight pointing angle of 0°. The reader will benefit from comparing these patterns against the sidelobe source case of Fig. 10. Figure 8(a) shows the distorted adapted left and right tracking beams, where the right beam is particularly adversely affected because of its overlap with the three strong sources located at 15, 22, and 30°. Figure 8(b) shows the resultant, distorted, adapted sum and difference tracking beams (a plot of W_s and W_d as given in Eqs. (65, 66)), where we note that the sum beam has been shoved over to the left and the difference beam has almost lost its right positive lobe. Figure 8(c) is the associated spatial filter insertion loss over the tracking beam region, an expanded portion of Fig. 7. And, Fig. 8(d) illustrates the associated track angle estimate (Δ/Σ) distortion, computed from Eqs. (64, 65, 66). Note the cusp which occurs at the location of the strong 30 dB source. This is undesirable, of course, since it could result in ambiguous track angle estimates in that vicinity. However, the insertion loss plot tells us that it would be virtually impossible to see any target return from that vicinity and, therefore, one can disregard it.

A verification data point is included for our true target location of −4°. It was obtained from monopulse track angle estimates averaged over 16 trials. Figure 9 shows a representative plot of tracking angle estimate vs time in PRF periods, where an averaging factor of 10 is incorporated into the plot outputs to reduce the dispersion of the plot and to keep the various curves separated reasonably well. For example, each track angle estimate plot point is an average of the previous 10 monopulse track angle estimates computed for the range-gated target pulses. The + and − symbols represent Σ and Δ beam output samplings just prior to the target pulse. These samplings verify that the interference sources have been attenuated down to receiver noise level at the output; i.e., they should merge into random receiver noise with a mean of 0 dB.

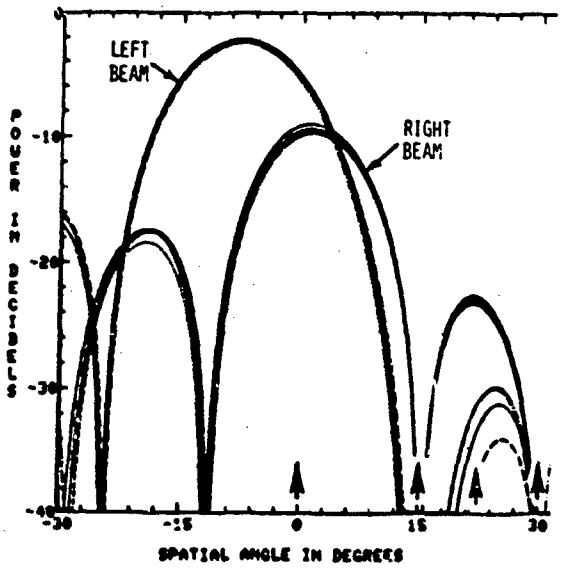

(a) Adapted tracking beams

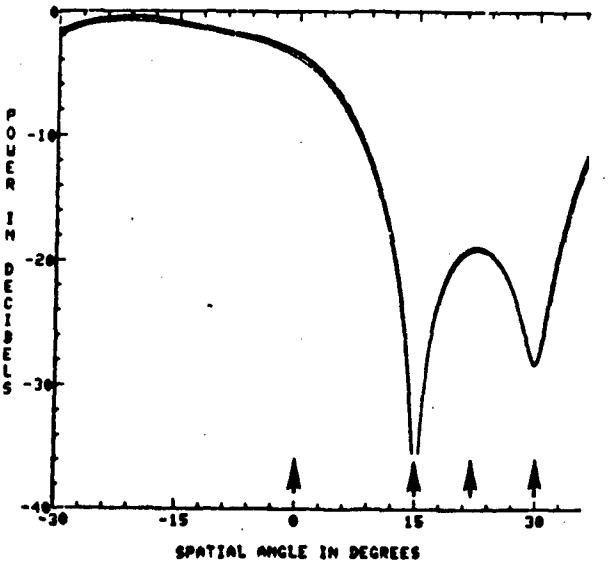

(c) Spatial insertion loss

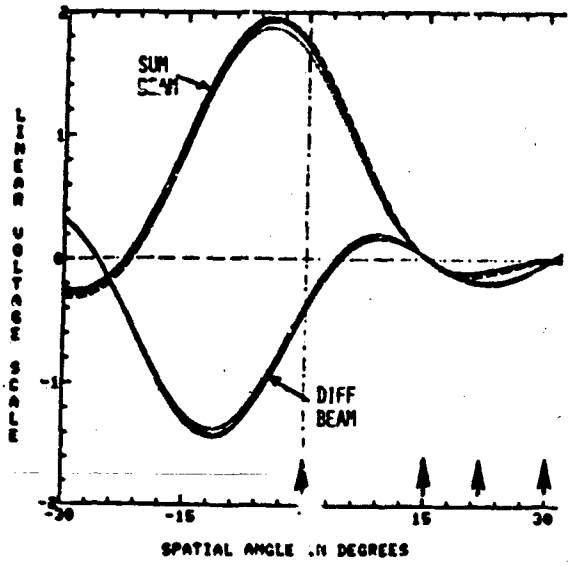

(b) Adapted sum and difference

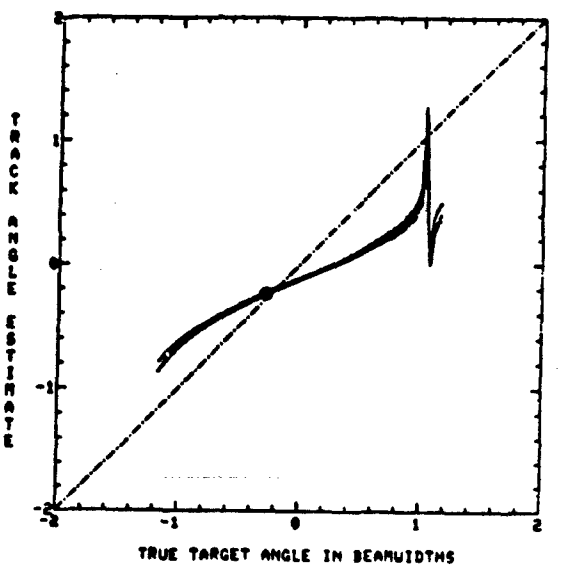

(d) Track estimate (Δ/Σ) distortion

Fig. 8 — Adaptive processing spatial filter functions related to tracking angle estimation for Case C8L6JVCϕB

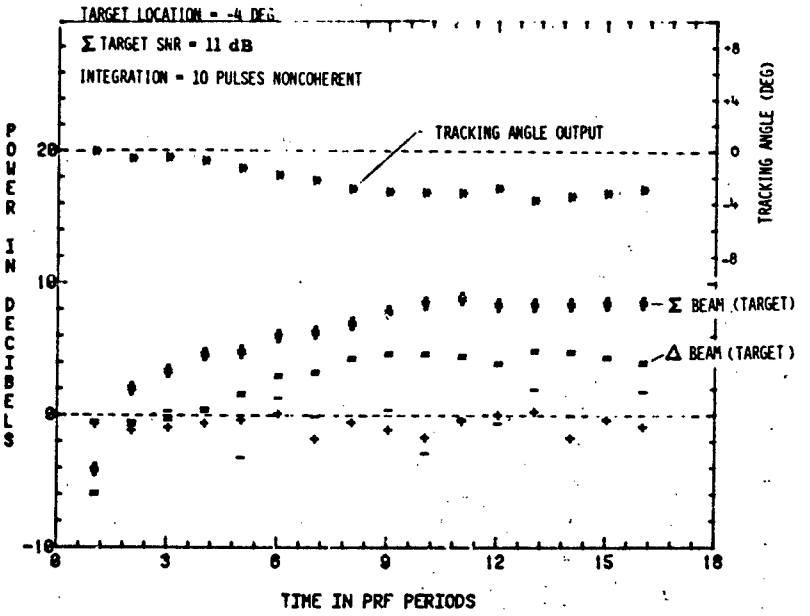

Fig. 9 — Time-sequence plots of sum beam output, difference beam output, and monopulse tracking angle estimate output for range-gated target pulses, 10-pulse noncoherent integration

3.2 Case C8L1JXX - One Source

These cases were designed to demonstrate how the track estimate distortion is affected by the position of the tracking beams with respect to the interference source. A single 7 dB SNR target appears in a single range bin per PRF period and is located within ±1 beamwidth of boresight. Table 1 contains the case identification numbers corresponding to the locations of a single 10 dB SNR interference source which appears in all range bins per PRF period. The tracking beams of our 8 element array have a boresight pointing angle of 0°, and a uniform illumination beamwidth $B = 14.5°$.

Table 1 — Case Identification Numbers

Case Number	Source Location	
	θ	(θ/B)
C8L1J8X	−30°	−2.0
C8L1J6X	−22°	−1.5
C8L1J4X	−14.5°	−1.0
C8L1J3X	−10.81°	−0.75
C8L1J2X	− 7.2°	−0.50
C8L1JϕX	0°	0

The simple block averaging method was used to compute $\hat{\mathbf{R}}$, with $N = 480$ snapshots, and the PEGS eigenanalysis algorithm was applied. Estimating a single source is almost trivial, and, as a result, showing the roots or the digital power/location estimates is not necessary.

One of the general characteristics demonstrated by this series of simulation tracking runs was that tracking beam distortion was rather negligible so long as the interference source remained in the sidelobe regions of the tracking beams, which is beyond approximately $\pm 22°$ for our example. Figure 10 illustrates this point for a source location of -2.0 beamwidths. Thus, distortion builds up only when the tracking main beams begin to overlap a strong source. Figure 11 illustrates a typical case where the interference source is located 0.75 beamwidth from boresight. Note the severe distortion of the left beam in Fig. 11(a) and the resultant distortion of the sum and difference beams in Fig. 11(b). A severe cusp occurs in the track estimate distortion of Fig. 11(d) at the position of the interference source, and this could lead to ambiguous track angle estimates in that vicinity. One solution to this ambiguity is to simply increase the filter insertion loss (Fig. 11(c)) where needed (similar to adding a synthetic interference source) so as to remove any possibility of a target return getting through on the wrong side. Figure 11(d) includes six verification data points for true target locations of -1.0, -0.5, -0.25, 0, $+0.5$, and $+1.0$ beamwidth. These points were obtained from monopulse track angle estimates averaged over 60 trials. Note that satisfactory tracking was obtained within 0.25 beamwidth of the interference source.

Figure 12 illustrates maximum distortion ambiguity which occurs for the special case when tracking beam boresight is directly steered onto a strong source. Tracking targets under this condition is not possible, and it obviously should be avoided.

3.3 Case C8L2J3C - Two Sources

The two-source cases were designed on the basis of results from the single source cases to demonstrate how the track estimate distortion is affected by the position of the tracking beams with respect to the two sources, particularly when the tracking main beams overlap the sources. The example chosen for presentation is like a superposition of Case numbers C8L1J6X and C8L1J3X from Table 1; i.e., there are two 10 dB SNR sources located at -1.5 and -0.75 beamwidths from tracking beam boresight.

Again, the processing involved simple block averaging to update $\hat{\mathbf{R}}$, with $N = 480$ snapshots; the PEGS eigenanalysis algorithm was applied, and the estimation of the two sources was easy because of their relatively large separation of 0.75 beamwidth.

Figure 13, which illustrates the resulting adaptive spatial filter functions, may be directly compared to Fig. 11 because of the identical location of the close source at -0.75 beamwidth. Note that there is some further degradation in all four plots on the left-hand side because of the presence of the second source, but that performance on the useful right-hand side has not been degraded. In fact, the track estimate distortion curve in Fig. 13(d) is now greatly improved because the possibility for ambiguity in the vicinity of the cusp has been removed by the insertion loss notch. Five verification data points are included for true target locations of -0.5, -0.25, 0, $+0.5$, and $+1.0$ beamwidth, averaged over 60 monopulse estimate trials. Again, satisfactory tracking was obtained within 0.25 beamwidth of the close source, which means that the target plus both interference sources were located within a beamwidth.

3.4 Case C8L3J3C - Three Sources

This case was designed by adding a third source between the above two sources; i.e., there are now three 10 dB SNR sources located at -1.5, -1.12, and -0.75 beamwidths from tracking beam boresight at 0°. The close spacing of 0.375 beamwidth between the three sources makes it a difficult case to estimate accurately; as a result, more processing results will be given for this example. Simple block averaging was again employed to update $\hat{\mathbf{R}}$ every 480 snapshots, and the SLC algorithm (Eq. (25)) and PEGS eigenanalysis algorithm were both applied.

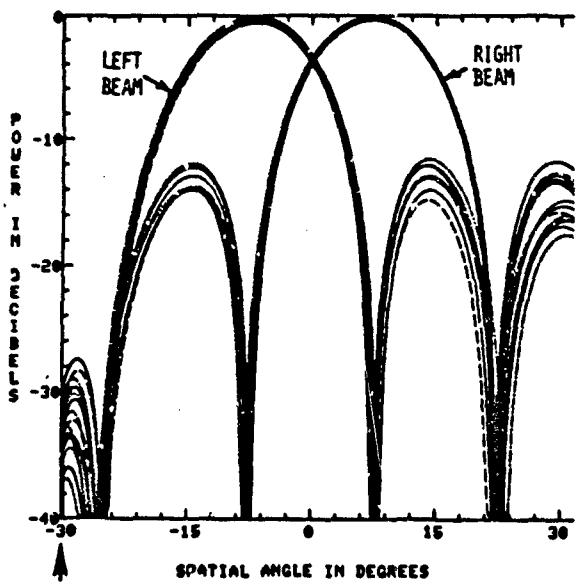

(a) Adapted tracking beams

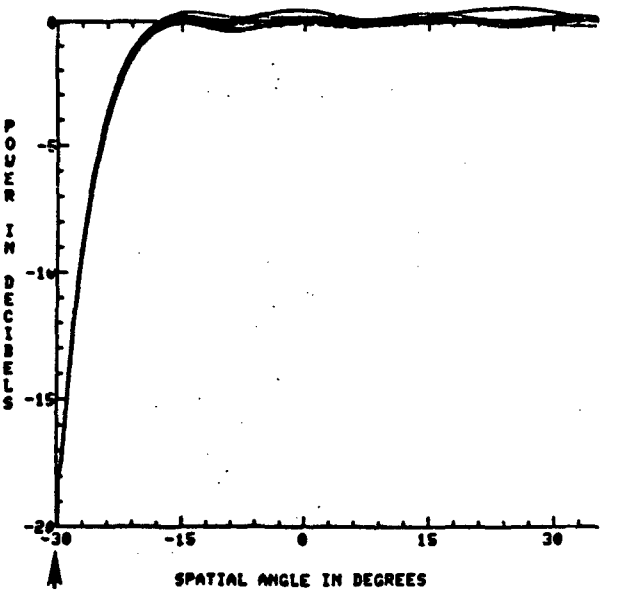

(c) Spatial insertion loss

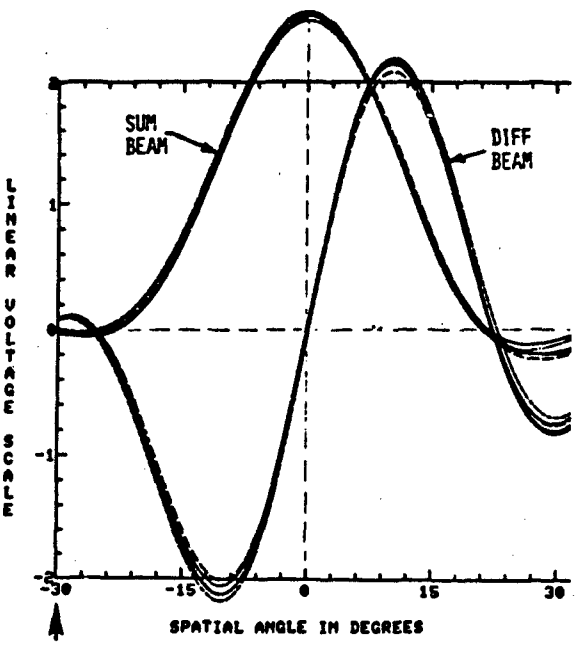

(b) Adapted sum and difference

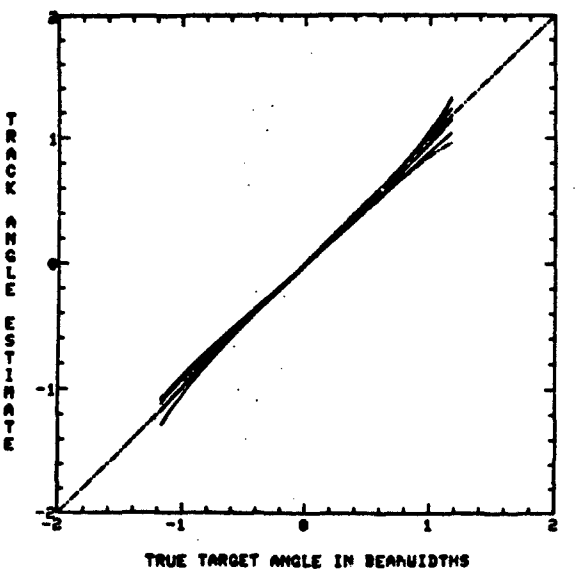

(d) Track estimate (Δ/Σ) distortion

Fig. 10 — Adaptive processing spatial filter functions related to tracking angle estimation for Case C8L1J8X

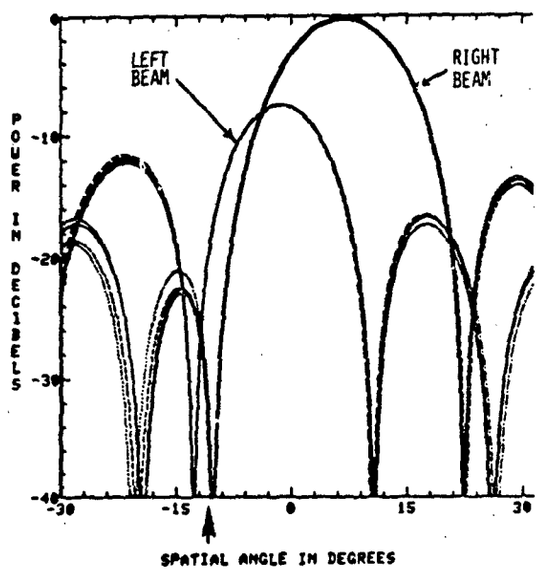

(a) Adapted tracking beams

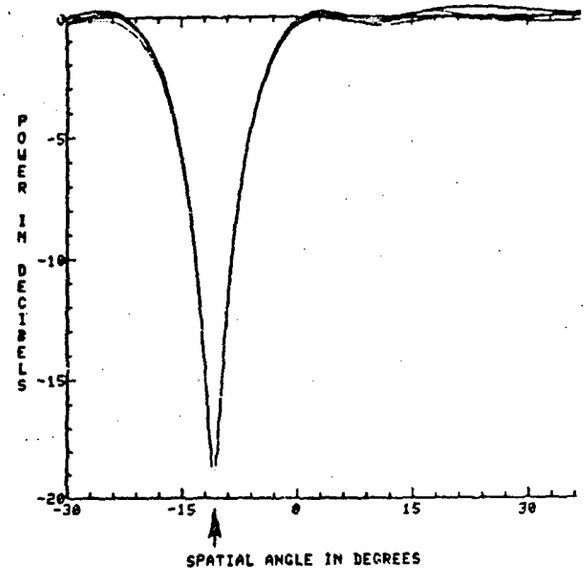

(c) Spatial insertion loss

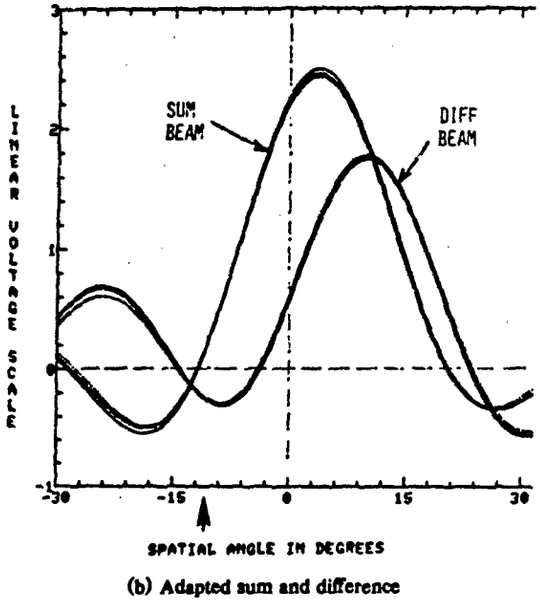

(b) Adapted sum and difference

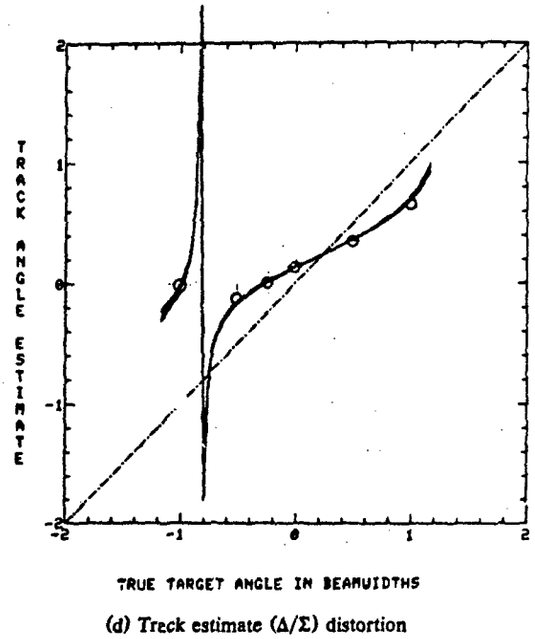

(d) Treck estimate (Δ/Σ) distortion

Fig. 11 — Adaptive processing spatial filter functions related to tracking angle estimation for Case C8L1J3A-I

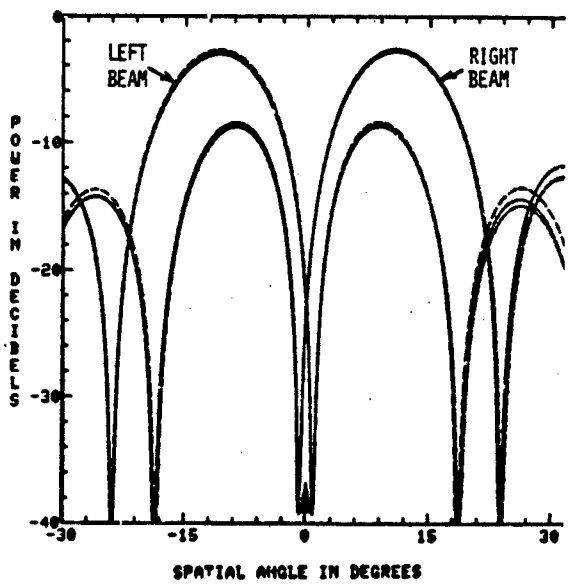

(a) Adapted tracking beams

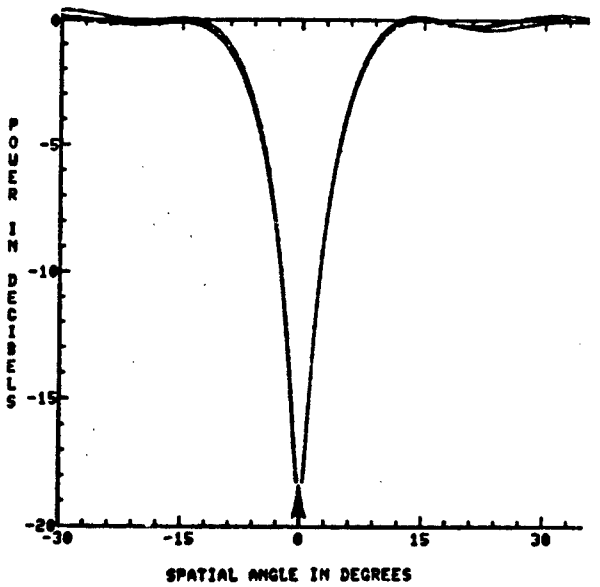

(c) Spatial insertion loss

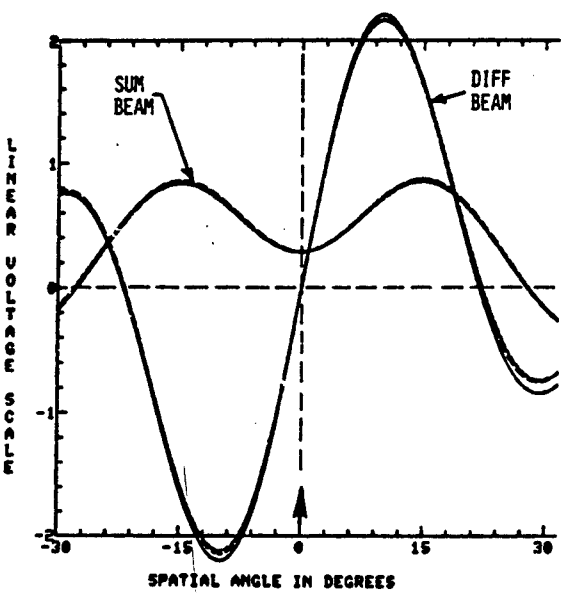

(b) Adapted sum and difference

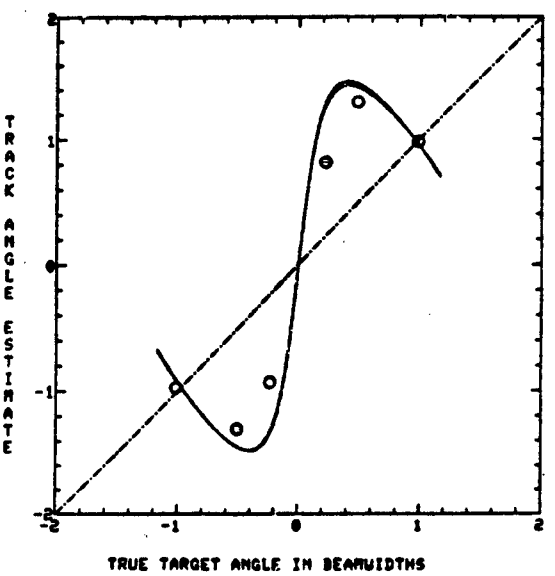

(d) Track estimate (Δ/Σ) distortion

Fig. 12 — Adaptive processing spatial filter functions related to tracking angle estimation for Case C8L1JϕA-I

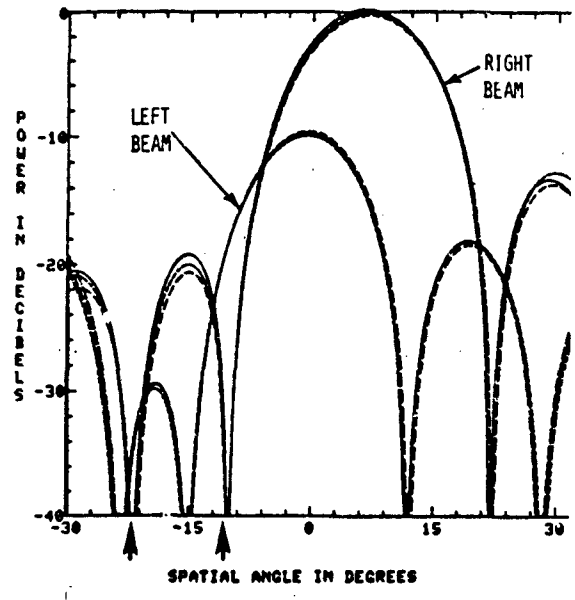

(a) Adapted tracking beams

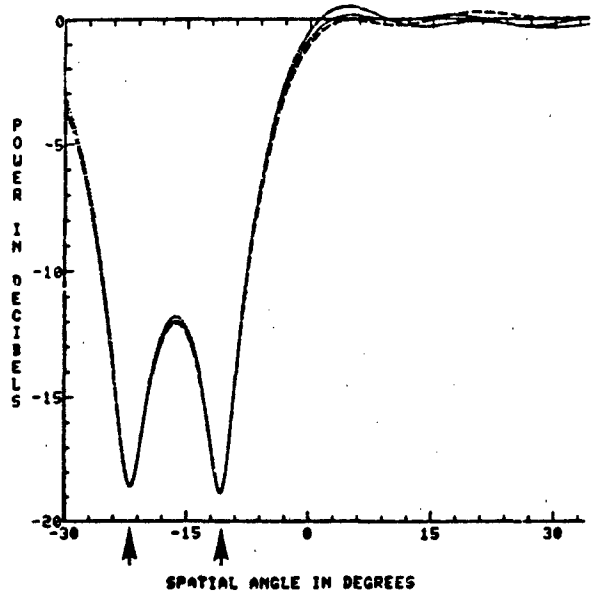

(c) Spatial insertion loss

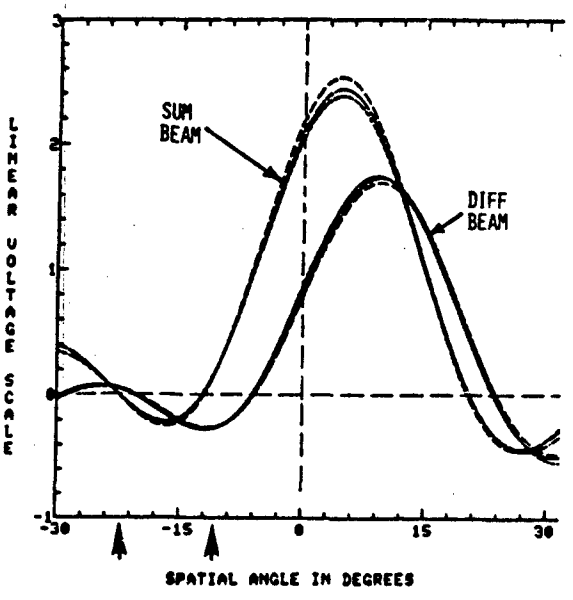

(b) Adapted sum and difference

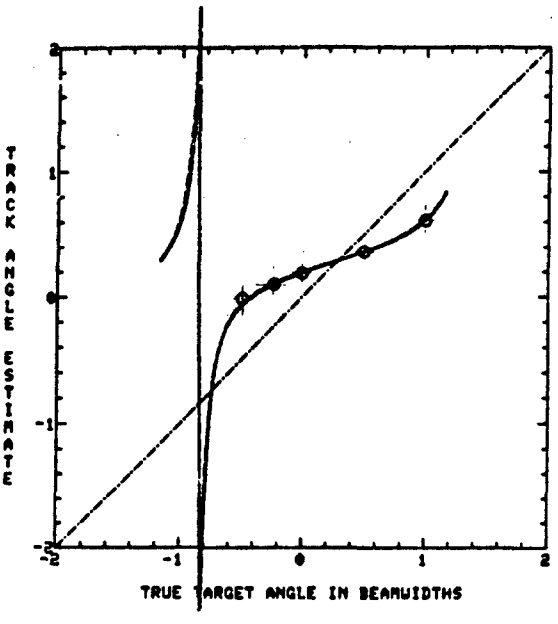

(d) Track estimate (Δ/Σ) distortion

Fig. 13 — Adaptive processing spatial filter functions related to tracking angle estimation for Case C8L2J3C-I

Rootfinding on the first eight updates of W_o from the SLC algorithm resulted in the Z-plane roots shown in Fig. 14(a). Note that only two roots are close to the unit circle, and these roots correspond to the two outer sources located at −22° and −10.8°. The SLC algorithm completely fails to resolve the third middle source.

By contrast, the PEGS eigenanalysis algorithm applied to the same eight $\hat{\mathbf{R}}$ updates results in the roots shown plotted in Fig. 14(b). Here, all three sources are readily resolved, and their roots hug the unit circle closely. Even the off-circle roots show considerably less scatter. The corresponding digital plot of estimated relative power vs estimated source location is shown in Fig. 15(a), where we note an accurate estimate of the power level of the third middle source in addition to its location. Figure 15(b) then illustrates the resulting filter insertion loss, computed for $\alpha = 1$.

Figure 16 shows a summary of the four adaptive spatial filter functions for tracking. In comparison to Figs. 11 and 13, note that only the left-hand side of the four plots shows any significant changes, and that the right-hand side of Fig. 16(d) is well protected from any cusp ambiguity because of the deep insertion loss notch extending over the entire interference source region. Five verification data points are included for true target locations of −0.5, −0.25, 0, +0.5, and +1.0 beamwidth, averaged over 60 monopulse estimate trials. A remarkable feature here is that satisfactory tracking has been obtained even with three strong interference sources located within a beamwidth of the target, i.e., the verification data point for the true target location of −0.5 beamwidth.

As an additional indicator of tracking results for this example, Fig. 17 illustrates a typical plot of track angle estimate vs time in PRF periods. An averaging factor of 10 is incorporated into the plot outputs to reduce the dispersion of the plot points and to keep the various curves separated reasonably well. For example, each track angle estimate plot point is an average of the previous 10 monopulse track angle estimates computed for the range-gated target pulses. The + and − symbols represent Σ and Δ beam output samplings just prior to the target pulse, and they serve to verify that the interference sources have been attenuated down to receiver noise level at the output; i.e., they should merge into random receiver noise with a mean of 0 dB.

3.5 Case C8L3J7B - Three Sources plus Spatial Noise

This case is included to illustrate the performance of the PEGS eigenanalysis algorithm when distributed background spatial noise (colored noise) is added to the previous three-source situation. The spatial noise in the simulation consisted of 35 random noise generators of −7 dB SNR level distributed uniformly in $\sin\theta$ space from −60° to 0°. Figure 18 shows the spatial spectrum estimates and the associated filter insertion loss obtained for the spatial noise alone, for eight trials of 480 snapshots each. Note that the PEGS algorithm estimates the distributed noise sources quite well by using five roots (degrees of freedom) to cover that extensive spatial region; i.e., it estimates on the basis of its 8-element array-aperture resolution capability. The insertion loss plot then provides the "envelope" outline of the spatial block of background noise, somewhat similar to an upside-down version of a windowed Fourier transform. This information could be used to provide prewhitening spatial filtering of the background noise.

The addition of the three 10 dB sources at −10.8°, −16.3°, and −22° then results in the overall estimates shown in Fig. 19. Note that the PEGS algorithm continues to use only five roots in estimating the combined situation, but we can readily discern the superposition of the two sets of sources. Some detail is lost since the spatial width of the background noise has shrunk slightly, and the three 10 dB sources are estimated as two sources (Fig. 19(a)). This latter result occurs because the background noise degrades the relative SNR of the three sources. Overall tracking distortion effects did not greatly differ from Fig. 16.

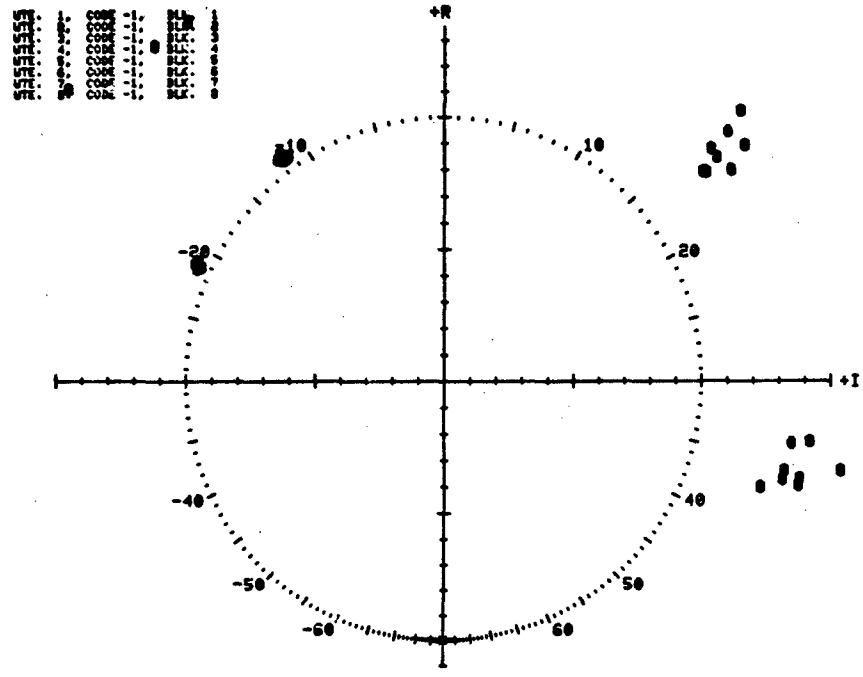

(a) SLC algorithm

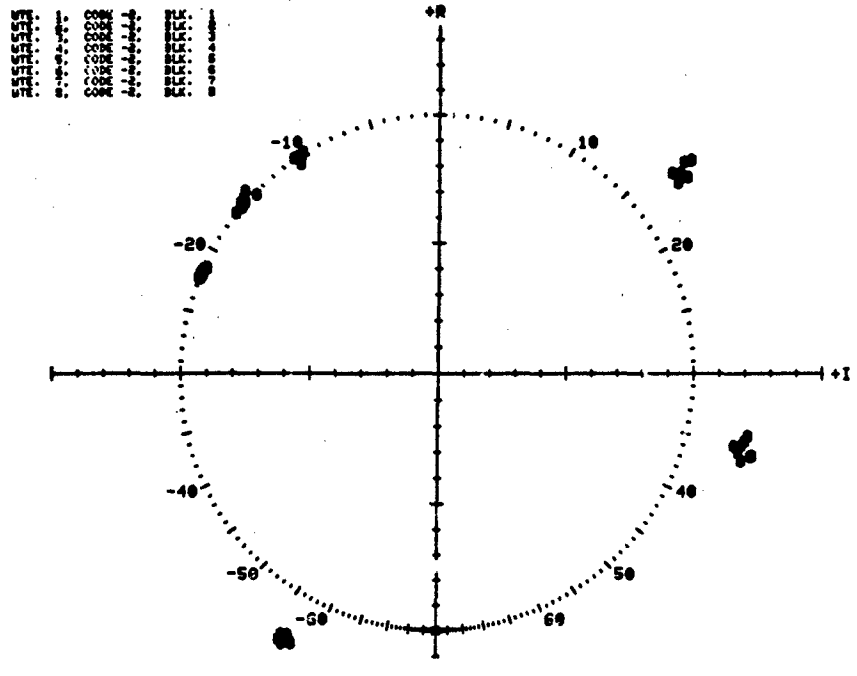

(b) PEGS eigenanalysis algorithm

Fig. 14 — Z-plane roots derived from optimum weights, eight trials of 480 snapshots each, Case C8L3J3C

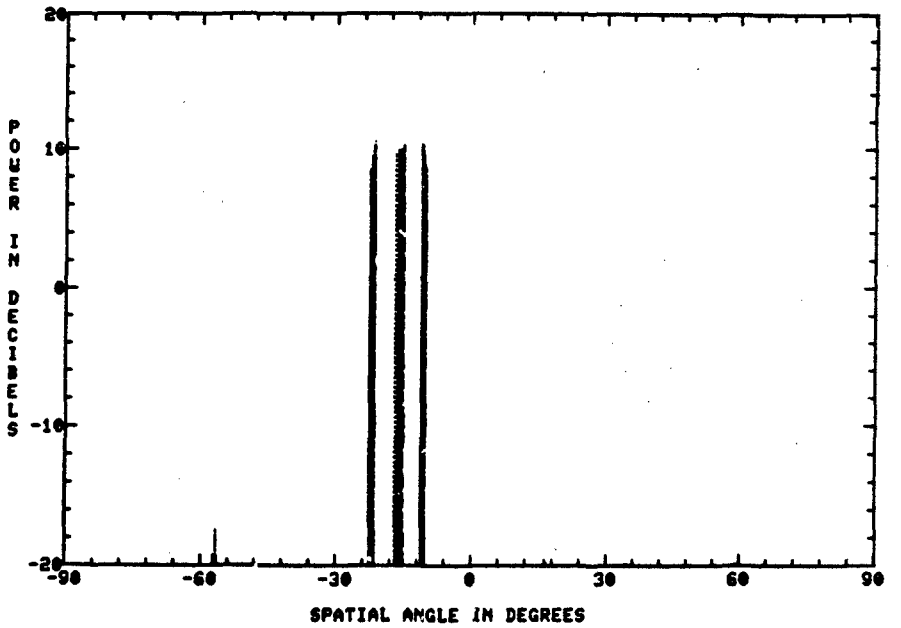

(a) Digital relative power vs location angle

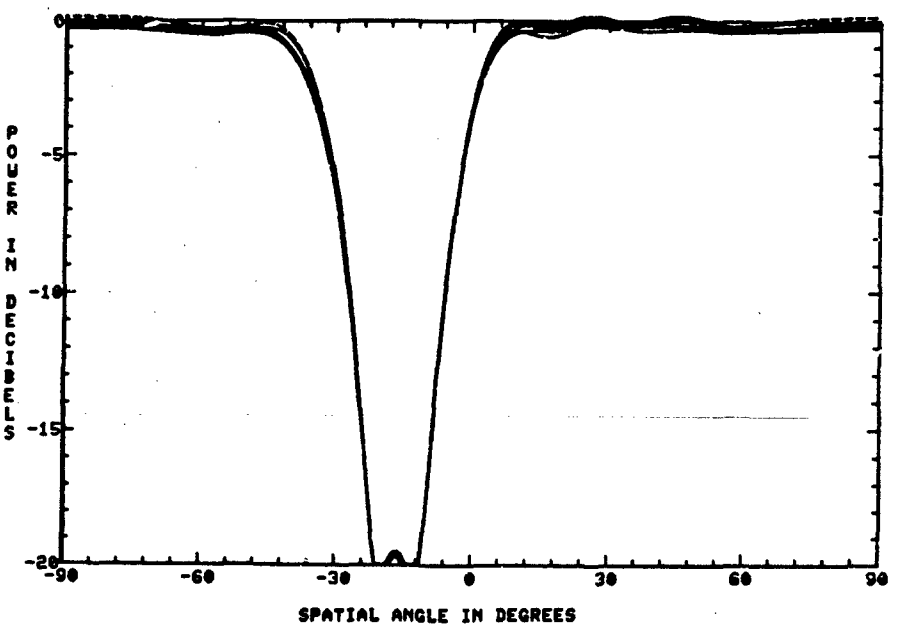

(b) Spatial filter insertion loss, $\alpha = 1$

Fig. 15 — Spatial spectrum estimates and associated filter insertion loss for Case C8L3J3C

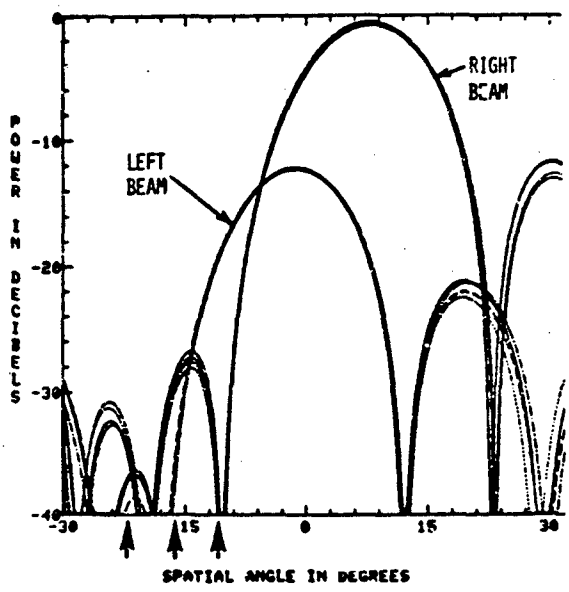

(a) Adapted tracking beams

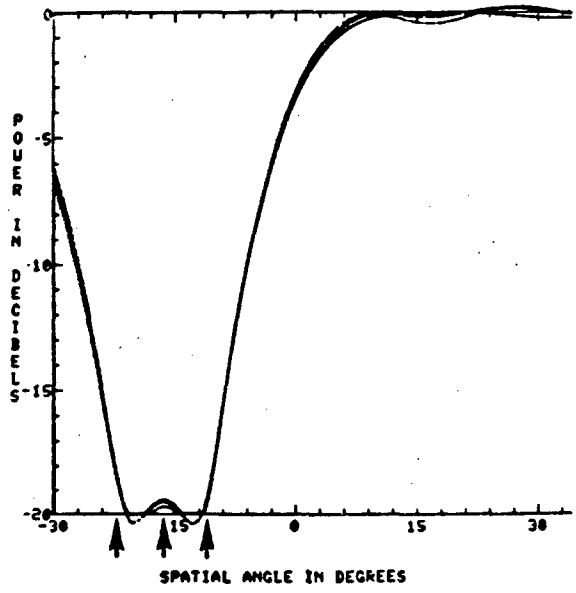

(c) Spatial insertion loss

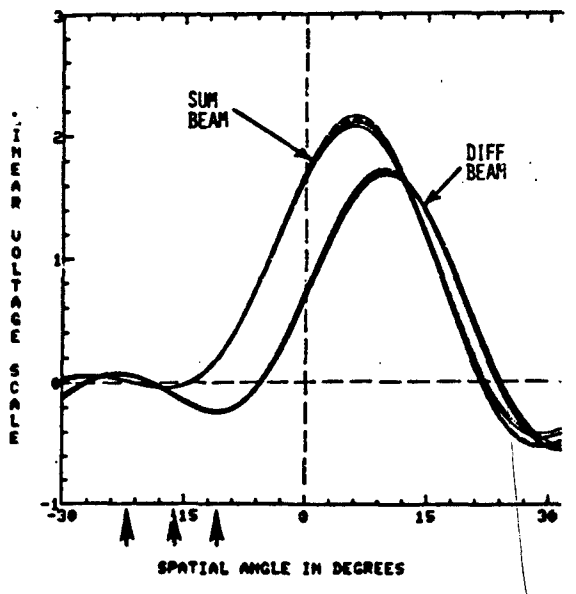

(b) Adapted sum and difference

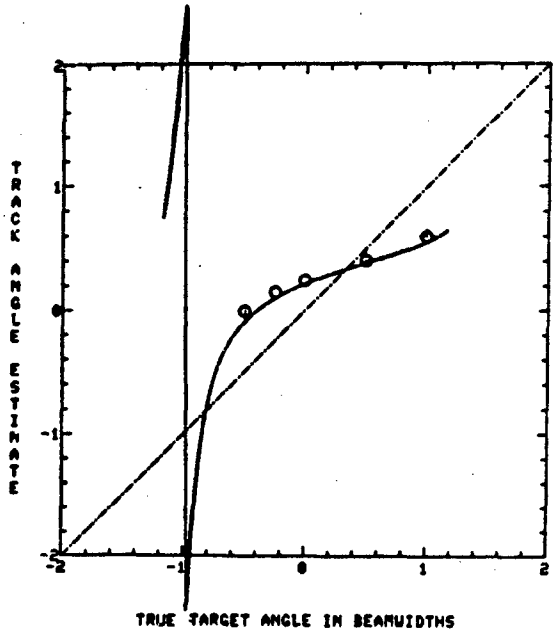

(d) Track estimate (Δ/Σ) distortion

Fig. 16 — Adaptive processing spatial filter functions related to tracking angle estimation for Case C8L3J3C-I

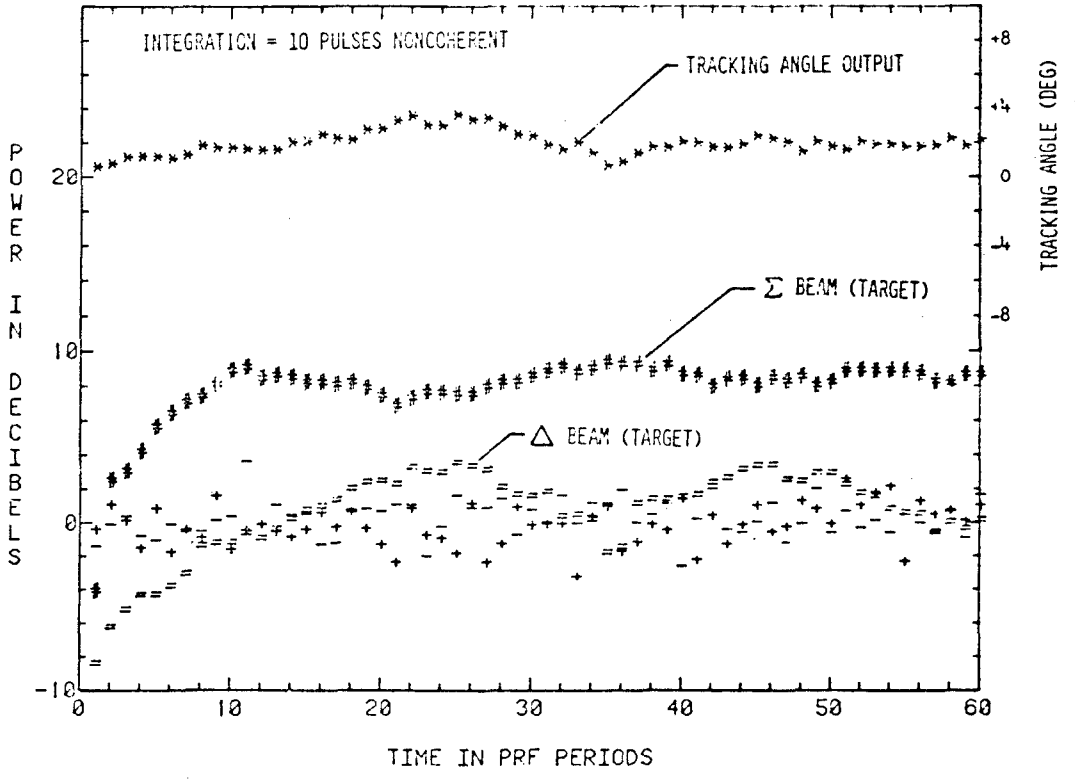

Fig. 17 — Time-sequence plots of sum beam output, difference beam output, and monopulse tracking angle estimate output for range-gated target pulses, 10-pulse noncoherent integration, Case C8L3J3D

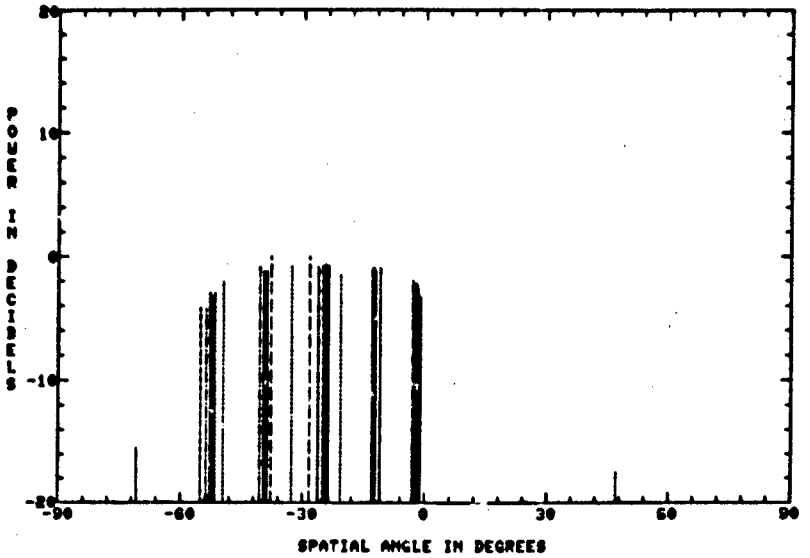

(a) Digital relative power vs location angle

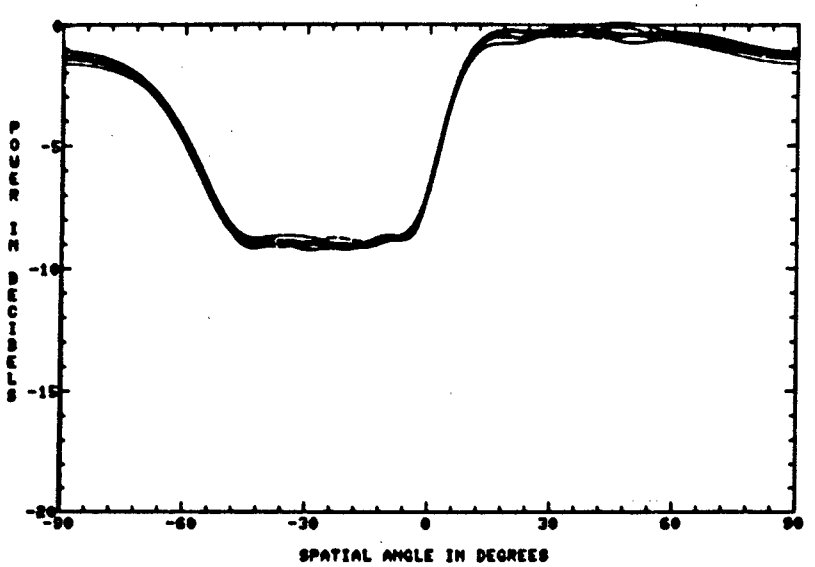

(b) Spatial filter insertion loss, $\alpha = 1$

Fig. 18 — Spatial spectrum estimates and associated filter insertion loss for Case CSL8JBG, eight trials of 480 snapshots each

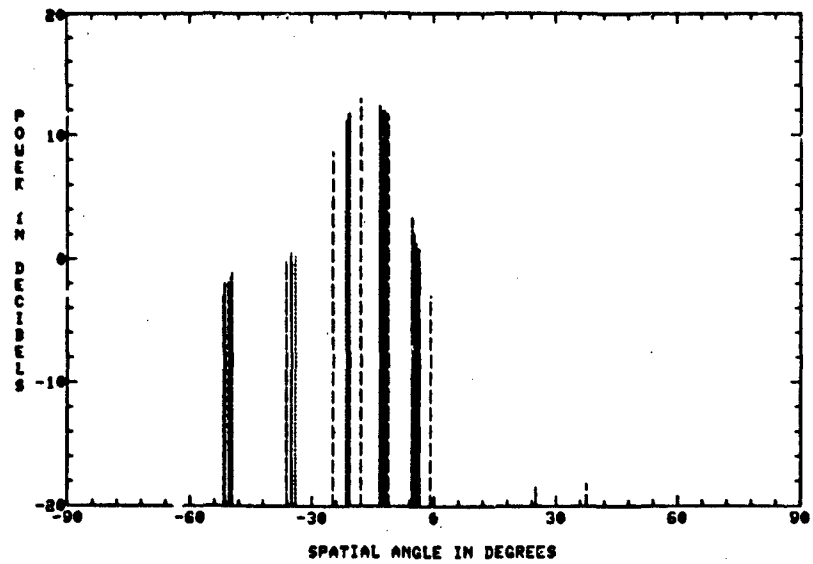

(a) Digital relative power vs location angle

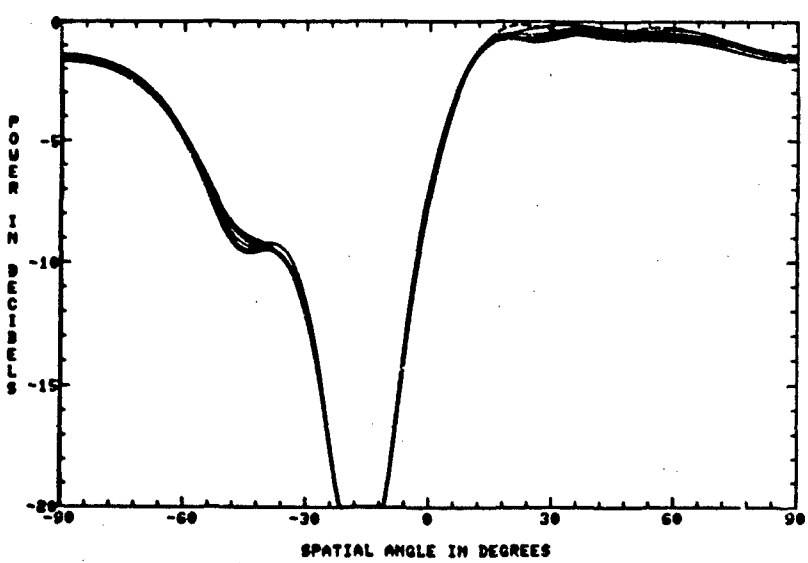

(b) Spatial filter insertion loss, $\alpha = 1$

Fig. 19 — Spatial spectrum estimates and associated filter insertion loss for Case C8L3J7B, eight trials of 480 snapshots each

4. ALGORITHM THEORY/ANALYSIS/DEVELOPMENT

A considerable number of algorithms in the literature could be applied to this problem area, but attention herein is focused primarily on eigenvalue/eigenvector decomposition techniques, sometimes referred to as principal eigenvector methods or singular value decomposition techniques. The reasons for preferring this class of algorithm is that these techniques demonstrate superior performance in the form of robustness against noise perturbations, maximum detection sensitivity, and maximum information potential. Adequate references are given below so that the reader may gain a better perspective of this rather broad technical area and may also consult more detailed presentations of the basic theory/analysis.

Computational load is generally higher with these techniques because of the eigenvalue/eigenvector evaluations involved. The particular computer code used by the author is a Fortran IV program called CMPLXE1G developed originally at the University of Wisconsin Computer Center [8]. Offsetting the increased computation, however, is the ever-increasing speed and capacity of modern CPU machines. In addition, rather efficient eigenvalue/eigenvector computation methods [9,10] exist which may be pursued if needed, and the impact of very large scale integrated circuits (VLSI) will undoubtedly soon be felt in modern signal processing.

4.1 Snapshot Signal Model

Adaptive response to a particular signal environment is based on algorithm-controlled processing of the sampled signals from multiple sensors. In this section we address the sampled signals by developing in detail a snapshot signal model which forms the basis for all computer simulations used in this report.

Consider a simple linear array of K elements as shown in Fig. 20. The received signal samples are correlated in both space and time, giving rise to a two-dimensional data problem, but we convert this to spatial domain only by assuming that narrow-band filtering precedes our spatial domain processing. Bandwidth can be handled when necessary via a spectral line approach [11] or tapped delay lines at each element [12], but we did not consider such extra complication essential to the basic purposes of this analysis. Thus, the postulated signal environment on any given observation consists of I narrow-band plane waves arriving from distinct directions θ_i. The RF phase at the kth antenna element as a result of the ith source would be the product $\omega_i X_k$, where X_k is the location of the element phase center with respect to the midpoint of the array in wavelengths, and ω_i is defined as

$$\omega_i = 2\pi \sin \theta_i. \tag{1}$$

This notation is deliberately chosen to have the spatial domain dual of sampling in the time domain, so that the reader may readily relate to the more familiar spectral analysis variables. Sin θ_i is the dual of a sinusoid frequency f_i, and the X_k locations are the dual of time sampling instants t_k. Note that if our elements are equally spaced by a distance d, then X_k may be written,

$$X_k = \left[\frac{d}{\lambda}\right]\left[k - \left[\frac{K+1}{2}\right]\right] \tag{2}$$

where λ is the common RF wavelength. The ratio d/λ becomes the dual of the sampling time T with the cut-off frequency equal to the reciprocal [13].

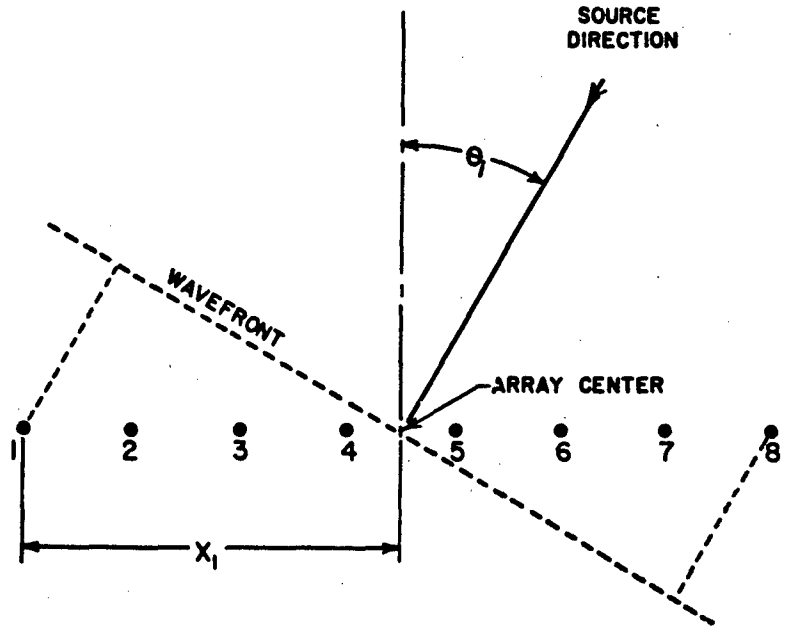

Fig. 20 — Geometry of linear array and signal wavefront

The complex amplitude of the l th source *at the array midpoint phase center* is p_l, such that we can now express the nth time-sampled signal at the kth element as,

$$E_k(n) = \eta_k(n) + \sum_{l=1}^{I} p_l(n) g_k(\theta_l) \exp(j\omega_l X_k) \tag{3}$$

where $g_k(\theta_l)$ is the element pattern response in the direction θ_l, and $\eta_k(n)$ is the nth sample from the kth element independent Gaussian receiver noise. (The receiver noise component is assumed to be a random process with respect to both the time index n and the element index k.) Equation (3) permits us to construct a convenient column vector of observed data in the form,

$$\mathbf{E}(n) = \mathbf{V}\mathbf{p}(n) + \boldsymbol{\eta}(n) \tag{4}$$

$$\begin{bmatrix} E_1(n) \\ E_2(n) \\ E_3(n) \\ \cdot \\ \cdot \\ \cdot \\ E_K(n) \end{bmatrix} = \begin{bmatrix} v_{11} & v_{21} & & v_{I1} \\ v_{12} & v_{22} & & v_{I2} \\ v_{13} & v_{23} & & v_{I3} \\ \cdot & \cdot & \cdots & \cdot \\ \cdot & \cdot & & \cdot \\ \cdot & \cdot & & \cdot \\ v_{1K} & v_{2K} & & v_{IK} \end{bmatrix} \begin{bmatrix} p_1(n) \\ p_2(n) \\ \cdot \\ \cdot \\ \cdot \\ p_I(n) \end{bmatrix} + \begin{bmatrix} \eta_1(n) \\ \eta_2(n) \\ \eta_3(n) \\ \cdot \\ \cdot \\ \cdot \\ \eta_K(n) \end{bmatrix}$$

where $\mathbf{V}$ is a $K \times I$ matrix containing a column vector $\mathbf{v}_l$ for each of the I source directions; i.e.,

$$v_{lk} = g_k(\theta_l) \exp(j\omega_l X_k). \tag{5}$$

Note that Eq. (4) separates out the basic variables of source direction in the direction matrix **V**, source baseband signal in the column vector $\mathbf{p}(n)$, and element receiver channel noise in the column vector $\boldsymbol{\eta}(n)$. The vector $\mathbf{E}(n)$ is defined as the nth snapshot, i.e., a simultaneous signal sampling across all K-array elements at the nth time instant. These snapshots would nominally occur at the Nyquist sampling rate corresponding to our receiver bandwidth [13], so that a radar-oriented person may view them as range bin time samplings. However, for source estimation purposes, they need not necessarily be chosen from contiguous range bins and, in fact, for most applications it would be highly desirable to selectively time gate the snapshots used for source estimation. For this simple analysis, let us postulate that the snapshots are gated at more or less arbitrary instants of time.

Over typical processing intervals, the directions of arrival will not change significantly, so that **V** is a slowly changing matrix. In contrast, the signals $p_i(n)$ will generally vary rapidly with time, often unpredictably, such that we must work with their statistical descriptions. It is assumed that the signals are uncorrelated with receiver noise. Proceeding then from Eq. (4), we can obtain the covariance matrix **R** via application of the expected value operator $\mathscr{E}$, or ensemble average,

$$\mathbf{R} = \mathscr{E}[\mathbf{E}(n)\mathbf{E}^{*t}(n)] \tag{6}$$

$$\mathbf{R} = \mathbf{V}\mathbf{P}\mathbf{V}^{*t} + \mathbf{N} \tag{7}$$

where $\mathbf{N} = \mathscr{E}[\boldsymbol{\eta}(n)\boldsymbol{\eta}(n)^{*t}]$, $\mathbf{P} = \mathscr{E}[\mathbf{p}(n)\mathbf{p}(n)^{*t}]$, * is the complex conjugate, and t is the transpose. **N** is a simple diagonal matrix consisting of the receiver channel noise power levels. The diagonal elements of **P** represent the ensemble average power levels of the various signal sources, and off-diagonal elements can be nonzero if any correlation exists between the sources. Note that correlated far-field signals can easily arise if significant specular reflection or diffraction multipath is present.

4.2 Sample Covariance Matrix (SCM) Techniques

Antenna array snapshots are the fundamental input data to our processor, whether they are real measurements or computer simulated via the snapshot signal model developed in the previous section. They are generally used to computer update one of the following vectors or matrices kept in computer storage:

- Optimum weight vector. (Example—the Howells-Applebaum algorithm [14])
- Optimum weight matrix. (Example—the Gram-Schmidt algorithm [15])
- Sample covariance matrix (SCM). (To be discussed in this section)
- The Inverse of an SCM. (Example—Shapard et al. in Ref. 12)

This section addresses the SCM in some detail and, in particular, describes four different techniques that have been used in adaptive array processing:

1. simple block averaging,
2. time decay averaging,
3. sliding-window averaging, and
4. forward-backward subaperture averaging.

The SCM may be viewed as a repository of information gathered by the sampling antenna array, in which the individual covariance terms are estimates or averages derived from a finite number of data samples. In accordance with basic statistical theory [16], the accuracy of the covariance estimates improves as the number of data samples increases.

4.2.1 Simple Block Averaging

This is an SCM average taken over N snapshots, and may be expressed in the form,

$$\hat{\mathbf{R}} = \frac{1}{N} \sum_{n=1}^{N} [\mathbf{E}(n)\mathbf{E}(n)^{*t}]. \tag{8}$$

Characteristics: storage is required for the accumulating SCM, but not for the data snapshots; data, either before or after the block of N snapshots, are obviously not included; the value of N chosen must be large enough to obtain satisfactory estimates of the desired processing output quantities; as each block of N snapshots is completed, $\hat{\mathbf{R}}$ is passed on for further algorithm processing and a new SCM accumulation commences; the method works well for signal environments whose statistics change slowly and are satisfactorily integrated per choice of N.

4.2.2 Time Decay Averaging

This includes all previous data in the SCM average, but gives ever-decreasing weight to past data; i.e., it applies exponential time decay or "forgetting " of past data. Such decay averaging is the digital recursive equivalent of analogue filter integrator circuits. For example, the equivalent of a simple single-pole RC analogue integrator filter [17] may be expressed in the recursive backward-difference form,

$$\hat{\mathbf{R}}(n) = \left[\frac{\tau}{\tau + 1}\right] \left\{\hat{\mathbf{R}}(n-1) + \frac{1}{\tau} [\mathbf{E}(n)\mathbf{E}(n)^{*t}]\right\} \tag{9}$$

where $\hat{\mathbf{R}}(n-1)$ is the previous stored SCM and τ is a selectable integration time constant. Characteristics: storage is required for the previous SCM, but not for the data snapshots; all previous data are included, but with exponential time decay applied to the older data; the value of τ must be chosen large enough to obtain satisfactory integration; $\hat{\mathbf{R}}(n-1)$ is continuously available regardless of the value of n; i.e., it is always current; the method works well for signal environments whose statistics change slowly, but may not be suitable for abrupt bursts of signal because of the inherently long memory effect.

4.2.3 Sliding-Window Averaging

This is an SCM average taken over N snapshots, but here a window continually moves with the data in a "bumping" operation. A block of computer memory must be reserved for storage of the N previous snapshots,

$$\begin{bmatrix} \text{---} E(n-N) \text{---} \\ \vdots \\ \text{---} E(n-2) \text{---} \\ \text{---} E(n-1) \text{---} \end{bmatrix}. \tag{10}$$

When the current nth snapshot comes in, the entire data stack is bumped up by 1 such that the top "oldest" snapshot is bumped off the stack. In this method, one simply keeps the snapshot data stack current and computes the SCM only when needed,

$$\hat{\mathbf{R}}(n) = \frac{1}{N} \sum_{i=n}^{(n-N+1)} [\mathbf{E}(i)\mathbf{E}(i)^{*t}]. \tag{11}$$

Characteristics: storage is required for N data snapshots, but not for the SCM; after bumping off of the memory stack, old data is completely discarded; the value of N must be chosen large enough to obtain satisfactory integration; the SCM is computed only when needed; the method is well suited to signal environments whose statistics change rapidly or abruptly because of the finite-memory stategy and continuously updated snapshot data stack.

4.2.4 Forward-Backward Subaperture Averaging

This is an excellent technique for increasing the effective averaging of our SCM when needed, and it may readily be implemented if the antenna array elements are identical and equally spaced; Figure 21 illustrates this technique. We form a reduced dimension subaperture of L elements, where L must be less than the total number of array elements K. Starting from the left-hand side, the subaperture samples its first snapshot as elements 1 through L, then bumps to the right by 1 and samples its second snapshot as elements 2 through $(L + 1)$, then bumps to the right by 1 and samples its third snapshot as elements 3 through $(L + 2)$, etc. After bumping across to the Kth element, we will have accumulated $(K - L + 1)$ subaperture snapshots from one overall array data snapshot, such that we can increase our SCM averaging by that same factor. This subaperture motion from left to right produces what is generally termed "forward averaging." The technique may be applied to any SCM method. For example, the simple block averaging of Eq. (8) becomes

$$\hat{\mathbf{R}}_f = \frac{1}{N(K-L+1)} \sum_{n=1}^{N} \sum_{i=1}^{(K-L+1)} [\mathbf{E}(n,i)\mathbf{E}(n,i)^{*t}] \tag{12}$$

where $\mathbf{E}(n,i)^t = [E_i(n), E_{i+1}(n), \ldots, E_{i+L-1}(n)]$ and $\hat{\mathbf{R}}_f$ is the new reduced $L \times L$ dimension SCM. Note that $\mathbf{E}(n,i)$ may be expressed as the matrix product,

$$\mathbf{E}(n,i) = \mathbf{I}_i\mathbf{E}(n) \tag{13}$$

where $\mathbf{I}_i$ is a special $L \times K$ rectangular sampling matrix in which the i index denotes the first column where the identity matrix $\mathbf{I}$ begins. For example, the $\mathbf{I}_i$ matrix for $L = 3$, $K = 6$, and $i = 2$ would be,

$$\mathbf{I}_i = [\mathbf{O}|\mathbf{I}|\mathbf{O}]$$
$$\mathbf{I}_2 = \begin{bmatrix} 0 & 1 & 0 & 0 & 0 & 0 \\ 0 & 0 & 1 & 0 & 0 & 0 \\ 0 & 0 & 0 & 1 & 0 & 0 \end{bmatrix}. \tag{14}$$

An $\mathbf{I}_i$ matrix may be used to reduce the number of computations by multiplying the SCM of Eq. (8) to obtain

$$\hat{\mathbf{R}}_f = \frac{1}{(K-L+1)} \sum_{i=1}^{(K-L+1)} [\mathbf{I}_i\hat{\mathbf{R}}\mathbf{I}_i^t]. \tag{15}$$

Equations (15) and (12) give identical results, and both are mathematical expressions of the additional spatial averaging or "smoothing" that is obtained via the moving subaperture technique.

Furthermore, the averaging can be doubled again by reversing our subaperture at the right-hand side and bumping across to the left-hand side in similar fashion, but it requires conjugating the subaperture snapshots. This subaperture motion from right to left produces what is generally termed "backward-averaging." The reader can verify that the resulting SCM will be the conjugate transpose of

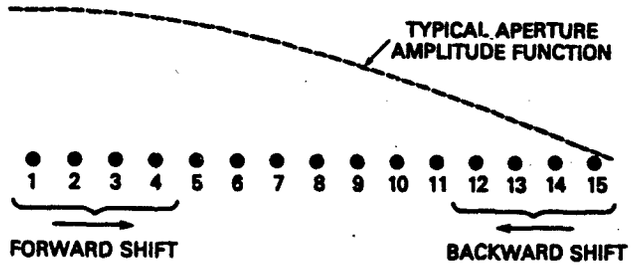

Fig. 21 — Forward-backward shift movement for a reduced dimension sampling subaperture where $L = 4$, along a linear antenna array of $K = 15$ elements

$\hat{\mathbf{R}}_f$, and that we can combine the two into a final forward-backward average SCM which is denoted as the reduced $L \times L$ matrix $\hat{\mathbf{R}}_{fb}$:

$$\hat{\mathbf{R}}_{fb} = \frac{1}{2}\,[\hat{\mathbf{R}}_f + \hat{\mathbf{R}}_f^{*t}]. \tag{16}$$

Note that $\hat{\mathbf{R}}_{fb}$ is a symmetric matrix, but is generally not Toeplitz. References 7, 18, 19 are recommended for further detailed discussion of the technique.

Although forward-backward subaperture averaging is a very simple concept, it usually produces remarkable improvements in output estimates and, in addition, becomes crucial to processing in the following situations:

- When only a few data snapshots are available per SCM computation. Note that the method can be used even under the extreme condition of only a single snapshot.
- When significant coherence exists between spatial sources as, for example, in multipath situations involving a specular reflection. For this particular condition, the fields arriving at the aperture are nonstationary in space and the SCM is not Toeplitz [1,5,19].

A caveat concerning this averaging technique is that, as the dimension L of the subaperture becomes smaller, the subaperture antenna gain, resolution, and degrees of freedom decrease. Thus, the advantage of increased averaging must always be balanced against these factors, and it is usually prudent to process with as large a subaperture dimension as possible.

4.3 Eigenvalue/Eigenvector Decomposition

When a signal is known to consist of pure sinusoids in white noise, an appropriate procedure to find the unknown frequencies and powers is the Pisarenko spectral-decomposition procedure [20]. Although Pisarenko's method per se has not found widespread use, it has provided a fundamental eigenanalysis basis for several closely related techniques which have demonstrated excellent performance. Among these are the algorithms described by Reddi [21], the MUSIC algorithm of Schmidt [22], the work of Bienvenu and Kopp [23], the singular value decomposition (or principal eigenvector) methods of Kumaresan and Tufts [24,25],the eigenassisted method of Evans et al. [19], and the algebraic approach of Bronez and Cadzow [26].

A key principle in all of these techniques is the geometric vector space relationships between the spatial source vectors and the eigenvectors of the sample covariance matrix; so we begin our discussion on this point. From the theory of matrices, we know that a positive definite Hermitian matrix such as $\mathbf{R}$ of Eq. (7) can be diagonalized by a nonsingular orthonormal modal matrix transformation which shall be defined as the matrix $\mathbf{Q}$. Furthermore, we know that the resulting diagonal components are the eigenvalues of matrix $\mathbf{R}$. In accordance with the usual eigenvalue problem statements,

$$|\mathbf{R} - \beta_i^2\mathbf{I}| = 0 \text{ and } \mathbf{R}\mathbf{e}_i = \beta_i^2\mathbf{e}_i, \tag{17}$$

the β_i^2 are the eigenvalues (real positive numbers) of **R**, **I** is the identity matrix, and $\mathbf{e}_i$ are the associated eigenvectors. These eigenvectors, which are normalized to unit Hermitian length and are orthogonal to one another, make up the columns of the **Q** matrix,

$$\mathbf{Q} = \begin{bmatrix} | & | & | & & | \\ \mathbf{e}_1 & \mathbf{e}_2 & \mathbf{e}_3 & \cdots & \mathbf{e}_K \\ | & | & | & & | \end{bmatrix} \text{ where } \mathbf{e}_i = \begin{bmatrix} e_{i1} \\ e_{i2} \\ e_{i3} \\ \cdot \\ \cdot \\ \cdot \\ e_{iK} \end{bmatrix}. \tag{18}$$

Diagonalization of **R** by the **Q** matrix transformation per Eq. (17) may be written,

$$[\mathbf{Q}^{*t}\mathbf{R}\mathbf{Q}] = [\beta_i^2\delta_{ij}] = \begin{bmatrix} \beta_1^2 & 0 & 0 & \cdot & \cdot & \cdot \\ 0 & \beta_2^2 & 0 & \cdot & \cdot & \cdot \\ 0 & 0 & \beta_3^2 & \cdot & \cdot & \cdot \\ \cdot & \cdot & \cdot & \cdot & & \\ & & & & \cdot & \\ \cdot & \cdot & \cdot & & \cdot & \\ & & & & & \\ \cdot & \cdot & \cdot & & & \beta_K^2 \end{bmatrix}, \tag{19}$$

where δ_{ij} is the Kronecker delta symbol. One can readily show a construction of **R** from its orthonormal components,

$$\mathbf{R} = \mathbf{Q}[\beta_i^2\delta_{ij}]\mathbf{Q}^{*t} = \sum_{k=1}^{K} \beta_k^2 \mathbf{e}_k \mathbf{e}_k^{*t}. \tag{20}$$

Next, we introduce the term "principal eigenvector" (PE) to mean those eigenvectors which correspond to the unique eigenvalues generated by the spatial source distribution; and the term "noise eigenvector" to mean those eigenvectors which correspond to the small noise eigenvalues generated by the receiver channel noise in Eq. (7). Under ideal conditions, the noise eigenvalues are all identical and equal to receiver channel noise power level β_o^2, such that we can factor Eq. (20) to emphasize the PE,

$$\mathbf{R} = \sum_{i=1}^{q} (\beta_i^2 - \beta_o^2)\mathbf{e}_i\mathbf{e}_i^{*t} + \beta_o^2\mathbf{I} \tag{21}$$

where q is the number of PE. Comparing Eq. (21) with Eq. (7) we note that the noise diagonal matrices are equal; i.e.,

$$\beta_o^2\mathbf{I} = \mathbf{N} \tag{22}$$

such that one may equate the source direction vectors with the PE,

$$\mathbf{VPV}^{*t} = \sum_{i=1}^{I} |\bar{p}_i|^2 \mathbf{v}_i \mathbf{v}_i^{*t} = \sum_{i=1}^{q} (\beta_i^2 - \beta_o^2)\mathbf{e}_i \mathbf{e}_i^{*t} \tag{23}$$

where the $|\bar{p}_i|^2$ represents the expected power levels of uncorrelated sources. Equation (23) embodies the key principle that the PE are linear combinations of the source direction vectors, and vice-versa. In geometrical language, the $\mathbf{v}_i$ define an I dimensional source vector space, and the principal $\mathbf{e}_i$ span that same vector space. Furthermore, since the noise eigenvectors are always orthogonal to the PE, then it follows that the noise eigenvectors must occupy a subspace which is orthogonal to the source vector space. To put it another way, if the noise eigenvectors are viewed as antenna array element weights, then they should have pattern nulls at source direction angles because of their orthogonality. Despite the fact that Eq. (23) is based on ideal assumptions, it turns out to be a valuable concept for formulating algorithms, perhaps because it is inherently a noise-subtracted relationship, and the estimates of the PE are rather robust.

When working with finite sets of data snapshots which are not ideal, a nontrivial problem area arises in determining which eigenvectors to designate as principal, and which ones result from noise. This important problem will be addressed after discussing the associated algorithms.

4.4 Eigenanalysis of Three Algorithms

Eigenvalue/eigenvector decomposition is now applied to three different spatial spectrum estimation algorithms to develop the particular algorithm which was chosen for processing sample covariance matrix data. Resultant source information derived from these algorithms directly determines the adaptive spatial filtering applied prior to target tracking. These algorithms are

- the MLM (Maximum Likelihood Method),
- the MUSIC (Multiple Signal Classification), and
- the PEGS (Principal Eigenvector Gram-Schmidt).

Since these algorithms are dealt with in a very abbreviated manner in this report, the reader is encouraged to consult the references given for a better description and understanding of the techniques involved.

4.4.1 The MLM (Maximum Likelihood Method)

The maximum likelihood spectral estimate is defined as a filter designed to pass the power in a narrow band about the signal frequency of interest and to minimize or reject all other frequency components in an optimal manner [4,27,28]. This is identical to the use of a zero-order mainbeam directional gain constraint in adaptive arrays [29,30], where the spatial spectrum would be estimated by the output residual power P_o from the optimized adapted array weights,

$$P_o(\theta) = \mathbf{W}_o^{*t}\mathbf{R}\mathbf{W}_o. \tag{24}$$

Where $\mathbf{W}_o$ is the optimum adaptive Wiener filter weight, and

$$\mathbf{W}_o = \mu\mathbf{R}^{-1}\mathbf{S}^* \tag{25}$$

where $\mathbf{S}^*$ is the usual mainbeam weight vector for steering angle θ, and μ is a complex number. Under the zero-order gain constraint, we require $\mathbf{S}^t\mathbf{W}_o = 1$, whereupon μ becomes

$$\mu = [\mathbf{S}^t\mathbf{R}^{-1}\mathbf{S}^*]^{-1}. \tag{26}$$

Substituting μ and $\mathbf{W}_o$ into Eq. (24) results in

$$P_o(\theta) = \left[\frac{1}{\mathbf{S}^t\mathbf{R}^{-1}\mathbf{S}^*}\right]. \tag{27}$$

Upon sweeping the steering vector $\mathbf{S}^*$ for a given covariance matrix inverse, $P_o(\theta)$ estimates the spatial spectrum.

In terms of eigenvalue/eigenvector decomposition, we can take the inverse of Eq. (19) and express $\mathbf{R}^{-1}$ in the form,

$$\mathbf{R}^{-1} = \mathbf{Q}\left[\frac{\delta_{ij}}{\beta_i^2}\right]\mathbf{Q}^{*t} = \sum_{k=1}^{K}\left[\frac{1}{\beta_k^2}\right]\mathbf{e}_k\mathbf{e}_k^{*t}. \tag{28}$$

Here, we see that this older algorithm simply uses all of the eigenvalues/eigenvectors. One advantage in this decomposition is that Eq. (28) can be substituted into Eq. (27) to form a simple summation of eigenvector beams referenced to the receiver noise power level,

$$\left[\frac{P_o(\theta)}{\beta_o^2}\right] = \frac{1}{\sum_{k=1}^{K}\left[\frac{\beta_o^2}{\beta_k^2}\right]g_k^2(\theta)} \tag{29}$$

where $g_k(\theta) = \mathbf{S}^t\mathbf{e}^k$. This permits an insight into the peak values which occur at the nulls of the noise eigenvector beams; i.e., we get an evaluation of relative source power level if the source location is resolved.

4.4.2 The MUSIC (Multiple Signal Classification)

This algorithm was suggested by Schmidt [22] to provide asymptotically unbiased estimates of the number of signal sources, directions of arrival, strengths and cross correlations among the directional waveforms, polarizations, and strength of noise/interference. His geometrical vector space description and interpretation is clearly presented and was used as the basis for Section 4.3 of this report. Essentially, this MUSIC algorithm selects and uses only the noise eigenvectors to solve for the directions of arrival. This is tantamount to approximating $\mathbf{R}^{-1}$ in Eq. (27) by the noise eigenvectors only, i.e.,

$$\text{let } \mathbf{R}^{-1} \approx \sum_{i=q+1}^{K}\left[\frac{1}{\beta_i^2}\right]\mathbf{e}_i\mathbf{e}_i^{*t} \tag{30}$$

where q is the number of principal eigenvectors. The same indexing would apply as noise eigenvector beams in Eq. (29), where we note that the ratio of eigenvalues would now become unity (or close to it).

This algorithm does indeed produce very large peaks in $P_o(\theta)$ for good covariance matrix estimates, because of the aforementioned orthogonality of the noise eigenvectors to the source vector space. Its performance is usually far superior to the older MLM algorithm in resolving closely spaced source directions. In addition, Schmidt points out that once the directions of arrival have been found, the direction matrix $\mathbf{V}$, in Eq. (4) and (7) becomes available and may be used to compute the source power matrix $\mathbf{P}$. We form the special matrix $\mathbf{U}$,
where

$$\mathbf{U} = [\mathbf{V}^{*t}\mathbf{V}]^{-1}\mathbf{V}^{*t} \tag{31}$$

and

$$\mathbf{UVPV}^{*t}\mathbf{U}^{*t} = \mathbf{P}.$$

If the matrix U exists or can be closely approximated, then we can apply it to the noise-subtracted covariance matrix of Eq. (7) to solve for P; i.e.,

$$\mathbf{P} = \mathbf{U}[\mathbf{R} - \mathbf{N}]\mathbf{U}^{*t} \tag{32}$$

$$\mathbf{P} = \begin{bmatrix} \overline{p_1^* p_1} & \overline{p_1^* p_2} & \cdots & \overline{p_1^* p_I} \\ \overline{p_2^* p_1} & \overline{p_2^* p_2} & \cdots & \overline{p_2^* p_I} \\ \cdot & \cdot & \cdot & \cdot \\ \cdot & \cdot & \cdot & \cdot \\ \cdot & \cdot & \cdot & \cdot \\ \overline{p_I^* p_1} & \overline{p_I^* p_2} & \cdots & \overline{p_I^* p_I} \end{bmatrix}.$$

Note that the diagonal elements of P represent power estimates of the sources, and that the nonzero off-diagonal elements represent estimates of the correlations existing between partially coherent sources.

The ability to solve for the power estimates is of great importance in distinguishing "false alarms" and in selecting the sources of interest. We recommend Refs. 19, 25, and 26 which are either related to or give a comparative analysis of the MUSIC algorithm.

4.4.3 The PEGS (Principal Eigenvector Gram-Schmidt)

Several eigenvalue/eigenvector decomposition techniques described in Refs. 19, 21, 25, and 26 are based on the principal eigenvectors (PE) together with some type of constraint imposed on the optimum weight vector.

This subgroup of PE methods is of interest in the current work because of their generally superior performance characteristics. An intuitive reasoning behind their use is that the estimates of the PE are robust; i.e., they tend to remain relatively stable from one data record to the next, whereas the noise eigenvectors tend to fluctuate because of noise perturbations. In addition, the PE methods are inherently a noise subtraction technique, similar to noise power cancellation algorithms which attempt to remove the noise bias term that appears along the main diagonal of the covariance matrix. Direct application of such reasoning is illustrated by the eigenassisted autoregressive (EAR) technique described in Ref. 19.

Let us begin development of our PEGS algorithm by decomposing the inverse of the covariance matrix as given in Eq. (28), normalized by receiver noise power,

$$\begin{aligned} \beta_o^2 \mathbf{R}^{-1} &= \sum_{k=1}^{K} \left[1 - \left[\frac{\beta_k^2 - \beta_o^2}{\beta_k^2} \right] \right] \mathbf{e}_k \mathbf{e}_k^{*t} \\ &= \mathbf{I} - \sum_{i=1}^{q} \left[\frac{\beta_i^2 - \beta_o^2}{\beta_i^2} \right] \mathbf{e}_i \mathbf{e}_i^{*t}. \end{aligned} \tag{33}$$

Substituting Eq. (33) into Eq. (25) results in the optimum Wiener weight,

$$\begin{aligned} \mathbf{W}_o &= \frac{\mu}{\beta_o^2} \left[\mathbf{I} - \sum_{i=1}^{q} \left[\frac{\beta_i^2 - \beta_o^2}{\beta_i^2} \right] \mathbf{e}_i \mathbf{e}_i^{*t} \right] \mathbf{S}^* \\ &= \mu' \left[\mathbf{S}^* - \sum_{i=1}^{q} \left[\frac{\beta_i - \beta_o^2}{\beta_i^2} \right] \alpha_i \mathbf{e}_i \right] \end{aligned} \tag{34}$$

where

$\alpha_l = \mathbf{e}_l^{*t}\mathbf{S}^*$,

$\mu' = \mu/\beta_o^2$, and

$\mathbf{S}^*$ = a quiescent array weight vector.

In the limit of noise-free data, Eq. (34) is suggestive of a simple Gram-Schmidt vector subtraction from $\mathbf{S}^*$ in which we would form an optimum weight that would be orthogonal to the PE and, therefore, orthogonal to the source direction vectors per Eq. (23). Thus, let us formulate such a PEGS algorithm by defining the optimum weight $\mathbf{W}_e$ from Eq. (34) as,

$$\mathbf{W}_e = \mathbf{S}^* - \sum_{l=1}^{q} \alpha_l \mathbf{e}_l \tag{35}$$

where

$$\alpha_l = \mathbf{e}_l^{*t}\mathbf{S}^*.$$

$\mathbf{W}_e$ possesses the necessary orthogonality to noise-free source direction vectors,

$$<\mathbf{W}_e, \mathbf{v}_l> = 0 \tag{36}$$

and may readily incorporate the option of unit Hermitian length if desired,

$$|\mathbf{W}_e|^2 = 1. \tag{37}$$

The PEGS algorithm as applied in this report used an end-element weighting for $\mathbf{S}^*$, i.e.,

$$\mathbf{S}^* = [0\ 0,\ \ldots,\ 0,\ 1]^t. \tag{38}$$

4.5 Culling Principal Eigenvalues

The number of principal eigenvalues is usually directly related to the number of sources which, in practice, are not known and must be estimated. One of the early estimation techniques which has often been used is the AIC (Akaike information criterion) [31,32]. This criterion has been successfully applied to many model identification problems in engineering and statistics, including the well known problem of determining the order of an autoregressive (AR) process [32]. Recent work reported by Wax and Kailath [33] presents a new approach, based on the AIC, which eliminates the need for any subjective judgment in the decision process; i.e., the procedure does not require any subjectively chosen threshold. This new approach was implemented during the current investigation and was found to be very effective for most of the examples tested. In addition to the Wax-Kailath AIC approach, we also used a second effective technique which is based on the following three processing operations:

- an initial decreasing-magnitude sort,
- culling per coarse magnitude threshold, and
- culling per sensitive threshold based on a quadratic curvefit predictor.

To explain these operations effectively, a typical example is analyzed.

Case C8L1J1TϕG consisted of an 8-element linear array with elements spaced half-wavelength, receiving signal on each snapshot from a 10 dB SNR source located at 0° and signal pulsed on every

64th snapshot from a 7 dB SNR source located at 6°, 480 snapshots of data used to form the sample covariance matrix, and a receiver noise power level of 17.64. Thus, the initial constants were

$K = 8$ (number of array elements),
$N = 480$ (number of snapshots), and
$\beta_o^2 = 17.64$ (receiver noise power level).

Computation of the eigenvalues for a simple block average SCM (Section 4.2.1) resulted in eight values which appeared in the initial sorting sequence as 1442.2, 23.8, 20.2, 19.9, 18.0, 17.5, 16.4, and 15.7.

The coarse magnitude threshold C_o is computed from the expression,

$$C_o = (1 + \alpha)\left[\beta_o^2 + \left(\frac{K}{2}\right) D_o\right] \tag{39}$$

where D_o is the average noise eigenvalue slope and α is a coarse magnitude threshold factor. The average noise eigenvalue slope can be readily determined from noise eigenvalue statistics as a function of the number of snapshots averaged in the sample covariance matrix. A satisfactory approximation for Eq. (39) has been found to be

$$D_o = \frac{\beta_o^2}{\sqrt{N}}, \tag{40}$$

which results in $D_o = 0.8$ for our example. The value of α must be chosen large enough to cover normal receiver noise statistical behavior, and 0.24 was found to be adequate. Substituting these values for our example results in a coarse magnitude threshold of $C_o = 25.9$, which culls out one principal eigenvalue from the initial sort. Note that β_1^2 agrees closely with the approximation for the two closely spaced sources.

$$\beta_1^2 \approx \left\{\left(|\bar{p}_1|^2 + \frac{|\bar{p}_2|^2}{64}\right) K + 1\right\}\beta_o^2. \tag{41}$$

Figure 22 shows the remaining eigenvalues and the coarse magnitude threshold value. The reader can verify that the average noise eigenvalue slope is very close to the value given in Eq. (40). The number of eigenvalues greater than C_o defines the initial value of our unique eigenvalue counter N_u so that we start with the initial count of $N_u = 1$.

Final culling is based on a sensitive magnitude threshold which is computed from a quadratic curvefit predictor applied to the next largest eigenvalue. In Fig. 22, that next value is 23.8 (the second eigenvalue), and we use the remaining six eigenvalues to evaluate the constants in a basic quadratic curvefit equation,

$$f(x) = ax^2 + bx + c \tag{42}$$

where x has an integer range of -5 to $+5$. A sliding window average is applied (when sufficient data values are available) and the data are weighted in accordance with the taper,

$$T(x) = \frac{1}{1 + \left(\frac{x}{5}\right)^2} \tag{43}$$

based on an 11-point window. The entire procedure is listed in the Appendix as a Fortran IV computer code.

Solution of Eq. (42) results in the fitted curve shown in Fig. 22, and gives us the predicted value of $\hat{\beta}_2^2 = 21.5$ in our example. The sensitive magnitude threshold consists of the inequality,

$$\text{if } (\beta_1^2 - \hat{\beta}_2^2) > 2.0\, D_c. \tag{44}$$

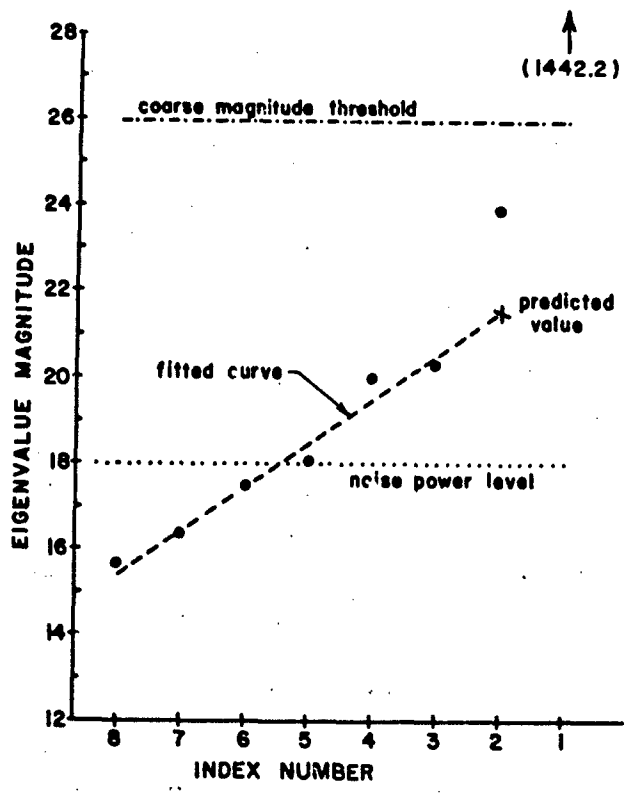

Fig. 22 — Plot of eigenvalues vs eigenvalue index for Case C8L1J1TϕG

This threshold is exceeded for the second eigenvalue, such that our unique eigenvalue counter is advanced to $N_u = 2$. Thus, we determine that there are two principal eigenvectors for our example case C8L1J1TϕG.

4.6 Rootfinding on the Optimum Weights

The spatial direction location angles of sources may be estimated by applying the conventional Fourier transform to evaluate zero locations of the optimum estimation weights, as illustrated in Fig. 4. However, a Fourier transform is restricted to the Z-plane unit circle by definition [13], and may not always provide adequate resolution of roots which migrate off the unit circle. A preferable method is that of solving for the exact roots of the array polynomial. For our purposes, this involves application of a rootfinding algorithm to the optimum estimation weights.

A listing of the Fortran IV computer code for the rootfinding algorithm used in this investigation is given in the Appendix. This algorithm may be used to find the roots Z_l of polynomials of the form

$$w_1 + w_2 Z + w_3 Z^2 + \ldots + w_K Z^{K-1} = 0 \tag{45}$$

where the w_k are complex array weight coefficients. The roots are found by expressing the polynomials in terms of Siljak functions and by using the method of steepest descent to determine the zeros [34]. Once a root is found, the polynomial is reduced by synthetic division and the process is repeated. The algorithm is very fast and robust.

Figure 23a illustrates an example of its application to Case C8L1J1TϕC, which consists of an 8-element linear array with elements spaced half-wavelength, a 10 dB source located at −8°, and a weak

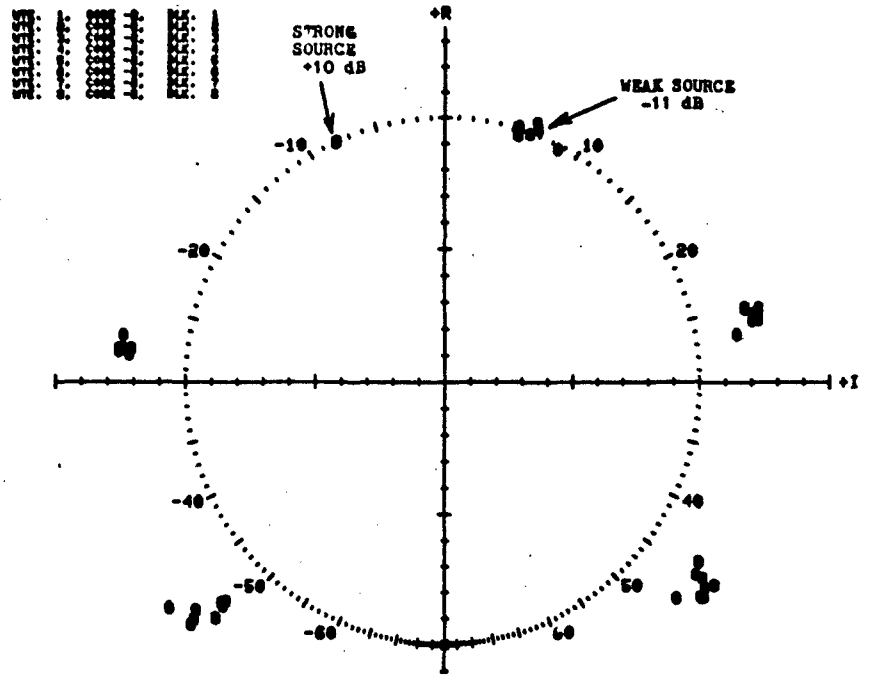

(a) Z-plane roots

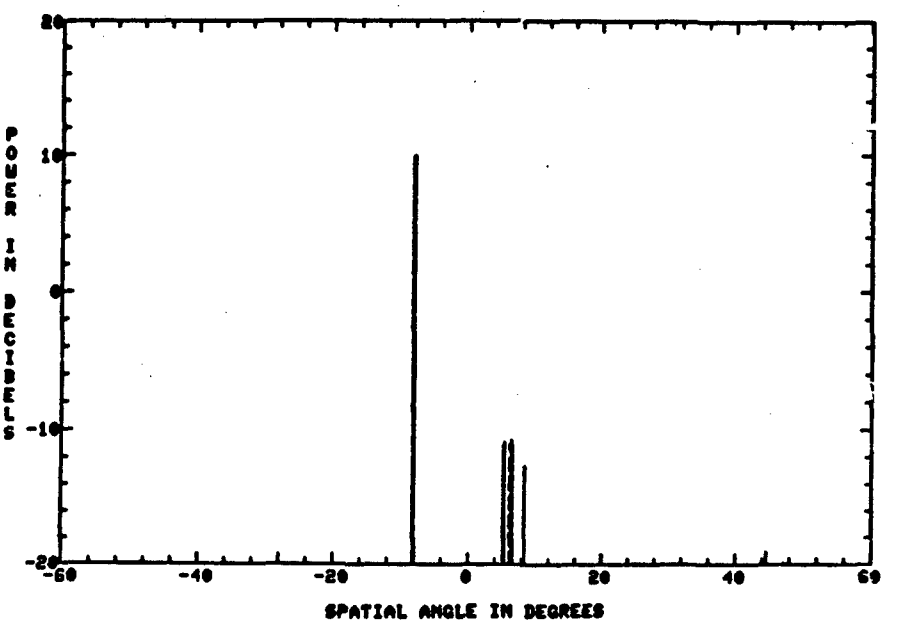

(b) Digital relative power vs location angle

Fig. 23 — Spatial spectrum estimates for Case C8L1J1TϕC, derived from PEGS eigenanalysis algorithm optimum weights, eight trials of 480 snapshots

−11 dB source located at +6°. Simple block averaging was used to accumulate a sample covariance matrix every 480 snapshots, and the PEGS algorithm was then applied to compute the optimum weights. The overlaid plots for eight successive trials demonstrate the following points:

- The strong 10 dB source is located accurately with very little variance.
- The weak −11 dB source shows appreciable variance in its location estimates, but note that its associated roots remain close to the unit circle.
- All remaining roots are well removed from the unit circle and may be disregarded, thus indicating that only two sources are present.

The deviation of the radial magnitude of roots from the Z-plane unit circle may be used as a coarse culling test to determine the number of sources present. A threshold value of 0.15 was selected for use with the PEGS optimum weight roots; i.e.,

$$\left|\,|Z_i| - 1\,\right| < 0.15. \tag{46}$$

After culling the roots in accordance with this coarse threshold, the associated source location angles are determined and used to construct the direction matrix **V** (Section 4.1). The ith root Z_i has the location angle θ_i

$$Z_i = \exp\,(j\pi \sin\theta_i) \tag{47}$$

and

$$v_{ik} = g_k(\theta_i)\,\exp\,(j\omega_i x_k),$$

where

$$\omega_i = 2\pi \sin\theta_i.$$

Knowing **V**, we can then solve for the source power matrix **P** as discussed in Section 4.4.2, Eqs. (31,32). Figure 23(b) illustrates a digital plot of resultant estimated relative power with respect to receiver noise power level vs estimated source location angles for the eight successive trials. A power level of −20 dB was selected for screening out "false alarms" which might get through the root culling, so this figure represents the end result of a triple source-screening processing, and gives us the final data:

Source	Location (deg)	Strength (dB)	Correlation
#1	−8	+10	0
#2	+6	−11	0
#3	0	0	0

4.7 Spatial Filter Weights

The target tracking concept shown in Fig. 2 permits great flexibility in updating the digital spatial filter weights because they are not developed simply as a closed-loop feedback adaptive response function. They are developed primarily on the basis of a model of the interference environment which is updated periodically via the estimated locations and relative power levels of sources which are logically determined to be interference. In addition, they can be modified by other inputs; for example,

- the addition of synthetic sources to reduce distortion ambiguities as discussed in Section 3.2, or to counter certain types of time-modulated interference;

- the option for "softened" spatial filtering as a trade-off to buy less tracking beam distortion, as discussed in this section and also Section 4.8;

- the option for time-modulated filter weights, including range-dependent control, to permit response to time/range dependent situations; and

- the option for real-time "clean-up" adaptive filter weight perturbations. These are based on feedback from the filter output residue signals, to permit fast response to interference source situations which are changing too rapidly for the relatively long periodic updates from the spectral estimation algorithms.

Therefore, let us begin by considering the construction of a full-aperture dimension estimated covariance matrix based on the signal source data applied to the model used for Eq. (7) in Section 4.1 above. Furthermore, let us solve for its eigenvalues/eigenvectors so that we may examine the formal eigenvalue/eigenvector spatial filter shown in Fig. 24. Here, we use a Q matrix beamformer to form the set of orthonormal eigenvector beams,

$$\hat{\mathbf{E}} = \mathbf{Q}^{t}\mathbf{E}. \tag{48}$$

Next, let us introduce an attenuation A_k for each beam output such that the attenuation is normalized to receiver noise power β_o^2; i.e.,

$$A_k = \left[\frac{\beta_o}{\beta_k}\right]^{\alpha} \tag{49}$$

where β_o is the square root of β_o^2, and β_k is the square root of the kth eigenvalue. We use α as an attenuation control parameter. When $\alpha = 1$, the output power of each attenuated beam will be equal to β_o^2, because the eigenvector beam output power is equal to its associated eigenvalue. Upon using a reverse beamformer to transform back to element space, we obtain the spatial filtered output residue signal vector,

$$\begin{aligned}\mathbf{E}_f &= \mathbf{Q}^{*}[A_k\delta_{kl}]\hat{\mathbf{E}} \\ &= \mathbf{Q}^{*}[A_k\delta_{kl}]\mathbf{Q}^{t}\mathbf{E}.\end{aligned} \tag{50}$$

Conventional beam weighting $\mathbf{S}^{*}$ can then be applied to the filtered output residue to obtain the beam output,

$$Y_o = \mathbf{S}^{*t}\mathbf{E}_f. \tag{51}$$

From Eq. (28) for the inverse of the covariance matrix, one can form an inverse which is normalized to receiver noise power,

$$\mathbf{M}^{-1} = [\beta_o^2\delta_{kl}]\mathbf{R}^{-1} = \mathbf{Q}\left[\frac{\beta_o^2}{\beta_k^2}\,\delta_{kl}\right]\mathbf{Q}^{*t}, \tag{52}$$

$$\mathbf{M}^{-1} = \mathbf{Q}[A_k\delta_{kl}]\mathbf{Q}^{*t} \text{ if } \alpha = 2. \tag{53}$$

Substituting the conjugate of Eq. (53) into Eq. (50), we may rewrite Eq. (51) in the form,

$$Y_o = \mathbf{S}^{*t}\mathbf{M}^{-1*}\mathbf{E} \tag{54}$$

and then use Eq. (25) to further express the filtered output residue in terms of the optimum adaptive Wiener filter weight,

$$Y_o = \mathbf{W}_o^{t}\mathbf{E}. \tag{55}$$

Thus, we have identical output from the optimum adaptive weights and the formal spatial filter of Fig. 24 when $\alpha = 2$.

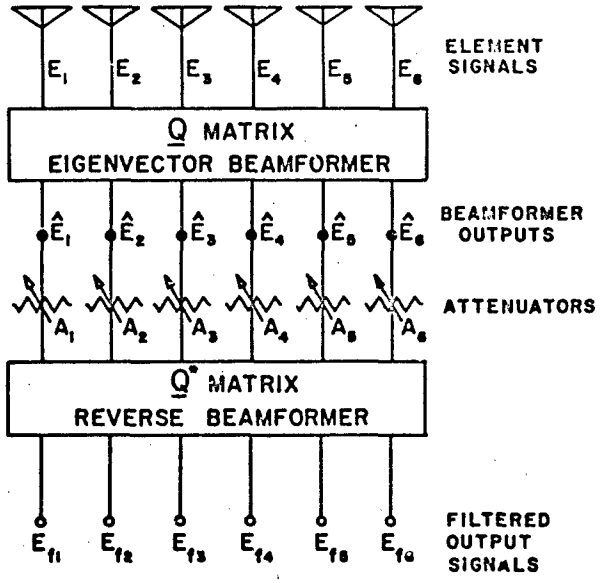

Fig. 24 — Formal eigenvalue/eigenvector spatial filter block diagram

The above discussion suggests a value range for the attenuation control parameter of

$$1 \leqslant \alpha \leqslant 2. \tag{56}$$

It must be emphasized that values of α less than 2 produce nonoptimal filtering. This condition is referred to herein as "softened" spatial filtering, because it reduces the spatial insertion loss below the value that would be obtained from optimum adaptive Wiener filter weights. Such softened insertion loss filtering is used as a trade-off option in the processing to buy less distortion of the target signals. Resultant degradation in the overall SNR is generally acceptable for most tracking situations, and readily reverted to optimal if needed.

The above discussion essentially presents two equivalent approaches for obtaining the spatial filter weights from the constructed covariance matrix:

- an eigenvalue/eigenvector solution and
- a matrix inverse solution

Note that the constructed covariance matrix permits options such as adding synthetic sources or reducing or increasing source power levels. Furthermore, since it is Toeplitz, solutions may be simplified in accordance with readily implemented schemes available in the literature. Other computational economies may be brought to bear via direct use of the known array polynomial roots.

4.8 Tracking Beams and Distortion

The tracking beams used throughout this report are based on selecting an adjacent pair of orthogonal, uniform-illumination beams such as those generated by a Butler matrix beamformer transformation, illustrated in Fig. 25. For example, the transformation matrix B for a linear array with an even number of equally spaced elements, will have individual matrix components of the form

$$b_{km} = \frac{1}{\sqrt{K}} \exp\left[\omega_t X_k + \frac{\pi}{2}\left[1 - \frac{2m}{K}\right](2k - K - 1)\right] \tag{57}$$

where

m = beam index (column),

k = element index (row),

X_k = element aperture location from midpoint,

$\omega_l = 2\pi \sin \theta_l$,

K = number of elements, and

$$\mathbf{B} = \begin{bmatrix} b_{11} & b_{12} & & b_{1K} \\ b_{21} & b_{22} & & b_{2K} \\ b_{31} & b_{32} & \cdots & b_{3K} \\ \vdots & \vdots & & \vdots \\ b_{K1} & b_{K2} & & b_{KK} \end{bmatrix}. \tag{58}$$

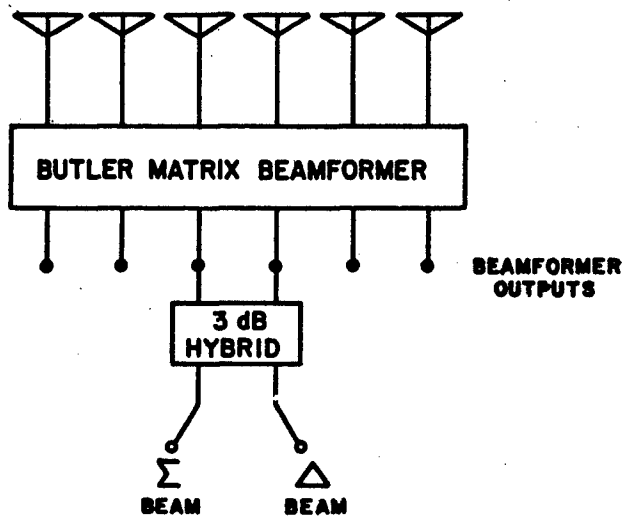

Fig. 25 — Block diagram of tracking beam formation via Butler matrix beamformer

Thus, the beamformer output vector $\hat{\mathbf{E}}$ may be expressed as

$$\hat{\mathbf{E}} = \mathbf{B}^t\mathbf{E} \tag{59}$$

where the columns of B are the individual beamsteering vector weights associated with each output beam. We select beam number ($K/2$) as our left beam of the pair, and angle θ_l as its pointing direction. Note that the selection automatically determines the pointing directions of all other beams. Figure 26(a) illustrates the sin x/x patterns of the left and right tracking beams (No. 4 and 5) for an 8-element linear array with half-wavelength spacing. The pointing direction relationship for these two beams may be written in terms of the Z-plane unit circle circumference segment,

$$\frac{2\pi}{K} = \pi(\sin \theta_{(l+1)} - \sin \theta_l), \tag{60}$$

and from this we can solve for the pointing direction of the right beam, the median boresight pointing direction for the pair, and the median beamwidth.

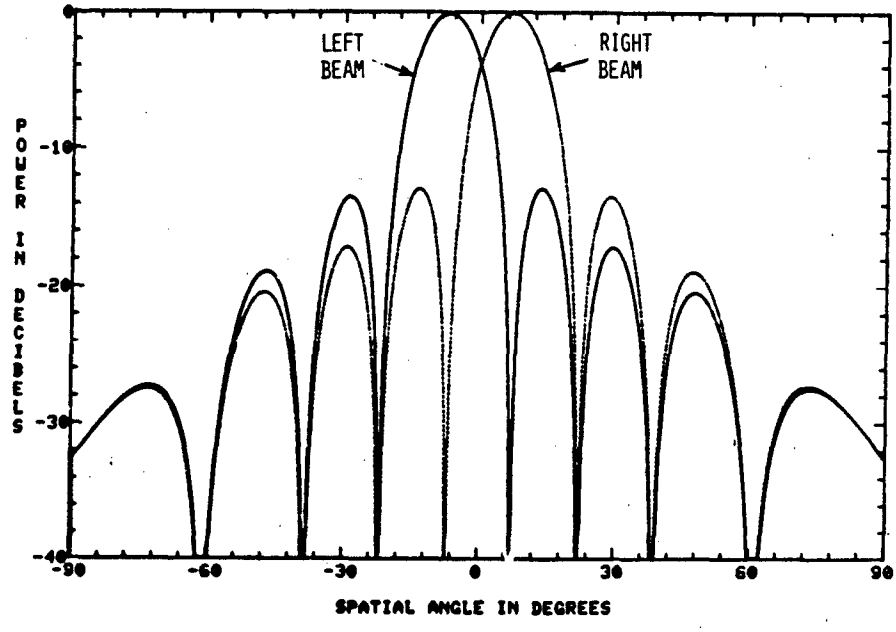

(a) Adjacent pair of Butler matrix beams

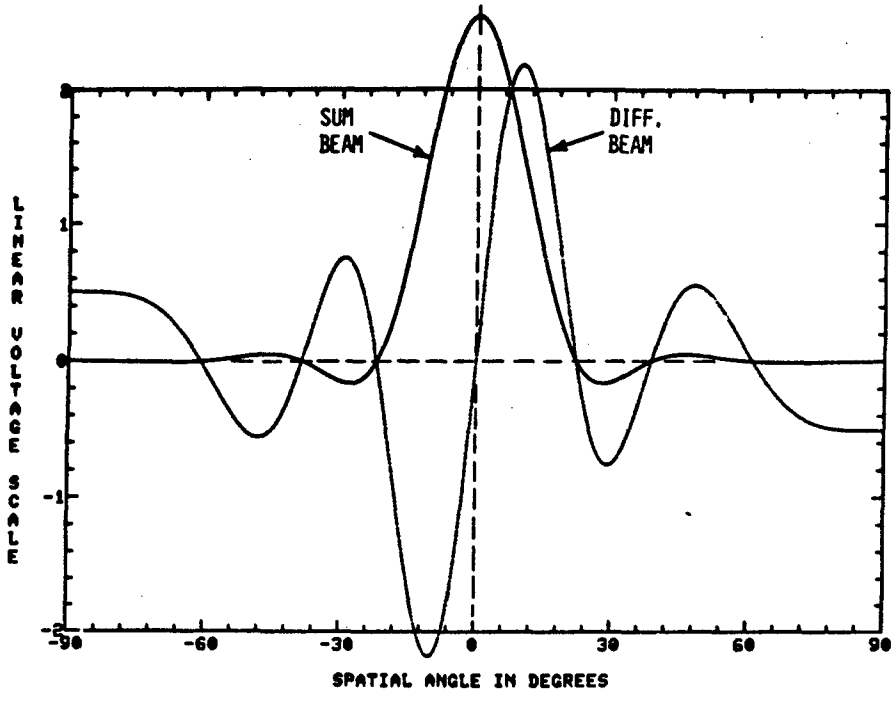

(b) Resultant Σ and Δ beams

Fig. 25 — Tracking beams formed for 8-element linear array

The familiar sum Σ and difference Δ tracking beam outputs are then obtained from this adjacent pair via the 3 dB hybrid junction shown in Fig. 25.

$$\Sigma = \frac{1}{2}\,[\hat{E}_{m+1} + \hat{E}_m]$$

$$\Delta = \frac{j}{2}\,[\hat{E}_{m+1} - \hat{E}_m] \tag{61}$$

where

$$m = (K/2),$$

and where we note that the difference beam is in quadrature phase relationship to the sum beam. Expressed in terms of equivalent element weights, the sum beam weight S and the difference beam weight D may be written via Eqs. (58,59)

$$\mathbf{S} = \frac{1}{2}\,[\mathbf{b}_{m+1} + \mathbf{b}_m]$$

$$\mathbf{D} = \frac{1}{2}\,[\mathbf{b}_{m+1} - \mathbf{b}_m]. \tag{62}$$

The uniform illumination vectors $\mathbf{b}_m$ and $\mathbf{b}_{m+1}$ result in cosine illuminations for S and D, which are readily computed for the beams of Fig. 26(a) as,

$$\mathbf{S} = \begin{bmatrix} 0.098 \\ 0.278 \\ 0.416 \\ 0.490 \\ 0.490 \\ 0.416 \\ 0.278 \\ 0.098 \end{bmatrix} \quad \text{and} \quad \mathbf{D} = \begin{bmatrix} -0.490 \\ -0.416 \\ -0.278 \\ -0.098 \\ 0.098 \\ 0.278 \\ 0.416 \\ 0.490 \end{bmatrix}. \tag{63}$$

These illuminations are shown plotted in Fig. 26(b) for our 8-element linear array example.

Monopulse tracking [35] involves an angle estimate for each pulse (snapshot) containing the target, and it is computed from the ratio of Δ/Σ. From the cosine illumination beams of Fig. 26, note that we can form the approximation,

$$\left(\frac{\Delta}{\Sigma}\right) \approx C\left(\frac{\sin\psi}{1+\cos\psi}\right) = C\,\tan\left(\frac{\psi}{2}\right) \tag{64}$$

where

$$\psi = \left(\frac{\pi}{2}\right)\left(\frac{\delta}{B}\right),$$

δ is the angle of the target from boresight,
B is the angle to the first null of the sum pattern, and
C is a constant which depends upon the particular illuminations.

For our example, $C = 3.8°$ and $B = 22.0°$. Thus, given values of Δ/Σ from Eq. (61), we can solve for the track angle estimates, δ/B, from Eq. (64).

Next, let us address track estimate distortion. Whenever one performs spatial filtering as described in Section 4.7, a distortion of received plane wavefronts occurs because the spatial insertion loss generally varies as a function of sin θ. This is shown in Eq. (50) which relates the filter output vector $\mathbf{E}_f$ to the filter input vector $\mathbf{E}$. The only condition under which $\mathbf{E}_f$ can retain the same phase slope as the input is when all of the A_k are equal. Such distortion can cause serious tracking errors from conventional sum and difference tracking beams.

This problem was first addressed in the literature by Davis, Brennan, and Reed [3], who proposed an algorithm for estimating the angle of arrival, based on the outputs of adaptively distorted sum and difference beams. They used approximations to the optimum angle estimator which permitted correction of distortion at the tracking beam boresight position, and they demonstrated good performance via simulation for sidelobe and/or mainbeam interference.

The approach we take here is that we know our adaptive filter weights, so that we can compute the resultant distortion error throughout the tracking beam region and use it directly for correction. In Section 4.7 above, we showed that it makes no difference whether we apply our quiescent beam weights to the spatially filtered signals, or the equivalent adaptive weights to the unfiltered signals. Thus, we may apply the monopulse sum and difference weights of Eqs. (62, 63) to the spatially filtered output residue signal vector of Eqs. (50, 51, 54, 55) and obtain the equivalent forms,

$$\Sigma = \mathbf{S}'\mathbf{E}_f = \mathbf{E}'\mathbf{M}^{-1}\mathbf{S} = \mathbf{E}'\mathbf{W}_s \tag{65}$$

and

$$\Delta = \mathbf{D}'\mathbf{E}_f = \mathbf{E}'\mathbf{M}^{-1}\mathbf{D} = \mathbf{E}'\mathbf{W}_d, \tag{66}$$

where $\mathbf{W}_s$ and $\mathbf{W}_d$ are now the equivalent adapted (and distorted) sum and difference beam weights. The distorted ratio Δ/Σ can be computed for any direction vector $\mathbf{E}$, thus giving us the necessary distortion correction curve across the entire tracking angle region.

If there are no interference sources, then spatial insertion loss is zero, there is no distortion, and we have the ideal linear track angle estimate case summarized in Fig. 27 for our 8-element array. Note that Fig. 27(d) is a plot of track angle estimate δ vs true target angle, as computed from Δ/Σ values obtained from Fig. 26(b) and plugged into Eq. (64). Linearity is excellent over the tracking region of ± 1 beamwidth. The abscissa scale in beamwidths is sized to correspond with the angle scale in degrees; i.e., the 3 dB beamwidth of our 8-element array is about 15°.

5. CONCLUSIONS

Two closely related new technologies, spectral estimation techniques and adaptive array processing techniques, have been applied to the radar systems problem area of tracking targets in the presence of nearby interference sources. It appears that the combination of these technologies does indeed offer some attractive possible solutions. This application area was addressed via an all-digital receive system concept whereby adaptive spatial filter weights are periodically updated on the basis of source estimates, and the filter output residue signals are then sifted for targets. Several simulation examples were included to illustrate some of the processing step outputs, "softened" spatial filter insertion loss, tracking beam distortions, correction for wavefront distortions, and satisfactory tracking in the presence of strong multiple interference sources located within a beamwidth of the target. Future plans include further evaluation of performance characteristics via more stringent/realistic computer simulations plus testing with experimental data.

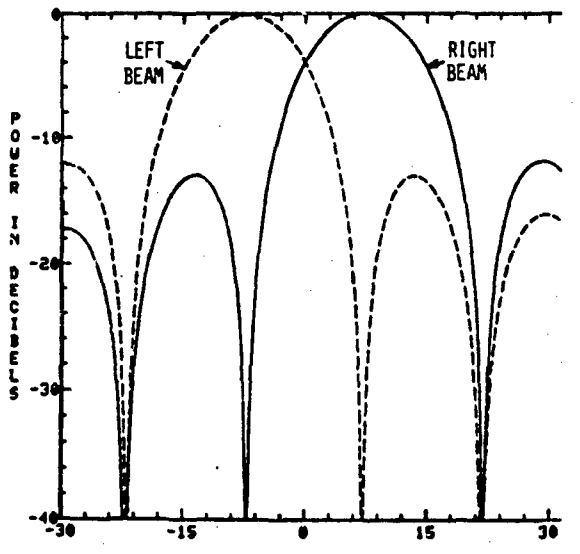

(a) Adapted tracking beams

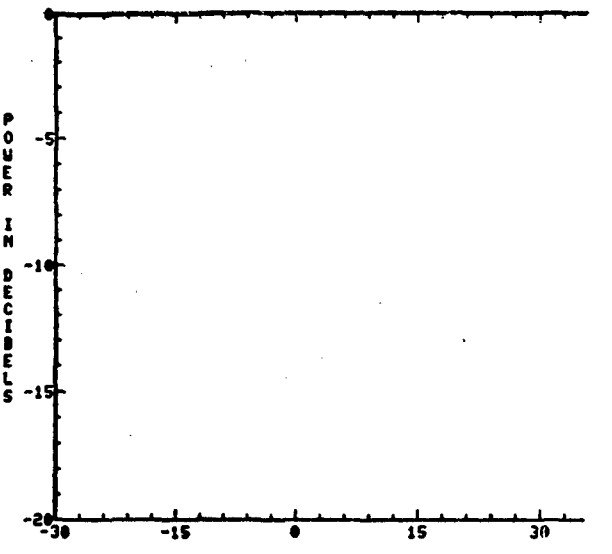

(c) Spatial insertion loss

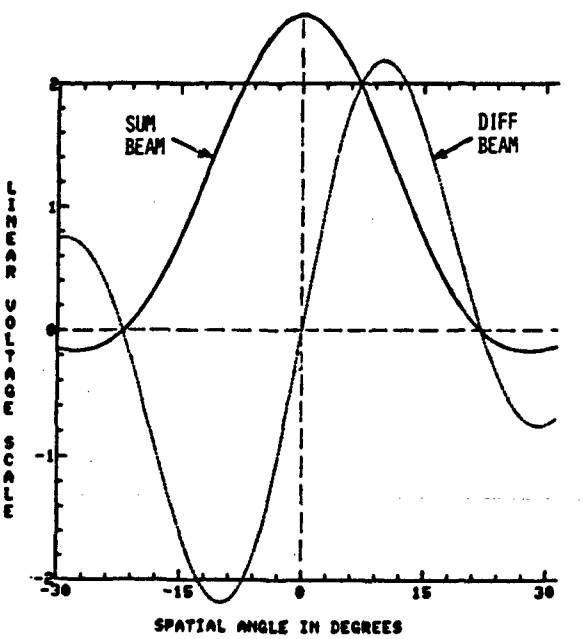

(b) Adapted sum and difference

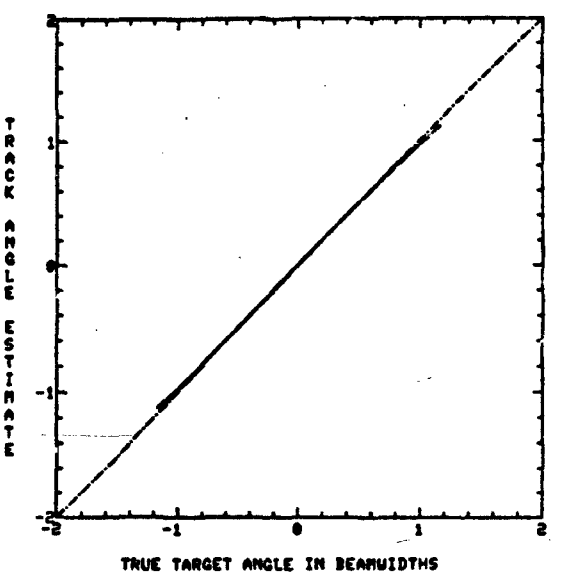

(d) Track estimate (Δ/Σ) distortion

Fig. 27 — Adaptive processing spatial filter functions related to tracking angle estimation for the ideal case of no interference sources

REFERENCES

1. W.D. White, "Low-Angle Radar Tracking in the Presence of Multipath," *IEEE Trans. AES*, AES-10, 835-853 (Nov. 1974).

2. B.H. Cantrell, W.B. Gordon, and G.V. Trunk, "Maximum Likelihood Elevation Angle Estimates of Radar Targets Using Subapertures," *IEEE Trans. AES*, AES-17, 213-221 (Mar. 1981).

3. R.C. Davis, L.E. Brennan, and L.S. Reed, "Angle Estimation with Adaptive Arrays in External Noise Fields," *IEEE Trans. AES*, AES-12, 179-186 (Mar. 1976).

4. W.F. Gabriel, "Spectral Analysis and Adaptive Array Superresolution Techniques," Proc. IEEE Vol. 68, June 1980, pp. 654-666.

5. W.F. Gabriel, "Tracking Closely Spaced Multiple Sources via Spectral-Estimation Techniques," NRL Report 8603, June 1982.

6. W. Chapman, S. Huber, T. Miller, "Mainbeam Notcher Program Final Report," AFSC Report No. F30602-81-C-0019, RADC, Contractor Hughes Aircraft Co., July 1982.

7. L. Marple, "A New Autoregressive Spectrum Analysis Algorithm," *IEEE Trans. ASSP*, ASSP-28, 441-454 (Aug. 1980).

8. Program CMPLXEIG, Univ. of Wis. Comput. Cen., Jan. 1966, UWCC ID Code B0018-00.

9. H.R. Schwarz, et al., *Numerical Analysis of Symmetric Matrices*, (Prentice-Hall, Englewood Cliffs, N.J., 1973), pp. 192-193.

10. J.N. Franklin, *Matrix Theory*, (Prentice-Hall, Englewood Cliffs, N.J., 1968), pp. 186-189.

11. W.F. Gabriel, "Adaptive Arrays—An Introduction," Proc. IEEE, 64, 239-272 (Feb. 1976).

12. L.E. Brennan, J.D. Mallett, and I.S. Reed, "Adaptive Arrays in Airborne MTI Radar," *IEEE Trans. Antennas & Propag.*, AP-24, 607-615, (Sept. 1976).

13. A.V. Oppenheim and R.W. Schafer, *Digital Signal Processing*, (Prentice-Hall, Englewood Cliffs, N.J., 1975).

14. S.P. Applebaum, "Adaptive Arrays," *IEEE Trans. Antennas Propag.*, AP-24, 585-598 (Sept. 1976).

15. M.A. Alam, "Orthonormal Lattice Filter—A Multistage, Multichannel Estimation Technique," *Geophysics*, 43, 1368-1383 (Dec. 1978).

16. A. Hald, *Statistical Theory with Engineering Applications*, (John Wiley & Sons, Inc., N.Y., 1952).

17. W.F. Gabriel, "Building Block for an Orthonormal-Lattice-Filter Adaptive Network," NRL Report 8409, July 1980.

18. A.H. Nuttall, "Spectral Analysis of a Univariate Process with Bad Data Points, via Maximum Entropy and Linear Predictive Techniques," NUSC-TR-5303, Naval Underwater Systems Center, New London, Conn., Mar. 1976.

19. J.E. Evans, J.R. Johnson, and D.F. Sun, "Application of Advanced Signal Processing Techniques to Angle of Arrival Estimation in ATC Navigation and Surveillance Systems," MIT Lincoln Laboratory Tech. Report 582, (FAA-RD-82-42), June 1982.

20. V.F. Pisarenko, "The Retrieval of Harmonics from a Covariance Function," *Geophys. J. (Royal Astron. Soc.)* **33**, 347-366 (1973).

21. S.S. Reddi, "Multiple Source Location - A Digital Approach," *IEEE Trans. Aerospace & Elect. Sys.*, **AES-15**, 95-105 (Jan. 1979).

22. R. Schmidt, "Multiple Emitter Location and Signal Parameter Estimation," Proc of the RADC Spectrum Estimation Workshop, RADC-TR-79-63, Rome Air Development Center, Rome, N.Y., Oct. 1979, p. 243.

23. E. Bienvenu and L. Kopp, "Adaptive High Resolution Spatial Discrimination of Passive Sources," *Underwater Acoustics and Signal Processing* (D. Reidel Publishing Co., Boston, 1981), pp. 509-515.

24. R. Kumaresan and D. Tufts, "Singular Value Decomposition and Spectral Analysis," Proc. of the First ASSP Workshop on Spectral Estimation, McMaster University, Hamilton, Ontario, Canada, Vol. 2, Aug. 1981, pp. 6.4.1-6.4.12.

25. R. Kumaresan and D.W. Tufts, "Estimating the Angles of Arrival of Multiple Plane Waves," *IEEE Trans. Aerospace & Elect. Sys.*, **AES-19**, 134-139 (Jan. 1983).

26. T.P. Bronez and J.A. Cadzow, "An Algebraic Approach to Superresolution Array Processing," *IEEE Trans. Aerospace & Elect. Sys.*, **AES-19**, 123-133 (Jan. 1983).

27. J. Capon, "High-Resolution Frequency-Wavenumber Spectrum Analysis," Proc. of IEEE, Vol. 57, Aug. 1969, pp. 1408-1418.

28. H. Cox, "Resolving Power and Sensitivity of Mismatch of Optimum Array Processors," *J. Acoust. Soc. Amer.* **54**(3), 771-785 (1973).

29. O.L. Frost, III, "An Algorithm for Linearly Constrained Adaptive Array Processing," Proc. IEEE, Vol. 60, Aug. 1972, pp. 926-935.

30. S.P. Applebaum and D.J. Chapman, "Adaptive Arrays with Main Beam Constraints," *IEEE Trans.*, **AP-24**, 650-662 (Sept. 1976).

31. H. Akaike, "Statistical Predictor Identification," *Ann. Inst. Statis. Math.* **22**, 205 (1970).

32. H. Akaike, "A New Look at the Statistical Model Identification," *IEEE Trans. Autom. Contr.* **19**, 716-723 (1974).

33. M. Wax and T. Kailath, "Determining the Number of Signals by Information Theoretic Criteria," Proc. of the IEEE/ASSP Spectrum Estimation Workshop II, Tampa, Fla., Nov. 1983, pp. 192-193.

34. J.B. Moore, "A Convergent Algorithm for Solving Polynomial Equations," *J. of the Assn. for Computing Machinery* **14**, 311-315 (Apr. 1967).

35. Merrill Skolnik, *Radar Handbook (McGraw-Hill Book, Co., N.Y., 1970).*

Appendix
FORTRAN IV COMPUTER CODE LISTINGS

1. DETERMINATION OF NUMBER OF UNIQUE EIGENVALUES

```
C  DETERMINATION OF NUMBER OF UNIQUE EIGENVALUES
C  FIRST APPLY COARSE MAGNITUDE LIMIT
      I0=0  ;FLAG FOR L0
      L0=0  ;NOISE EIGENVALUE COUNTER
      DO 74 N=1,NE0
      IF(EIG(N).GT.BL0)GO TO 74
      L0=L0+1
   74 CONTINUE
      IF(MOD(IP0,2).EQ.0)GO TO 88
   76 IF(L0.LT.2)GO TO 88  ;SKIP DIFF. LOOPS
C  NEXT DETERMINE DEVIATION FROM CURVEFIT
      J0=L0-11  ;NUMBER OF CURVEFITS ALLOWED
      IF(J0.GT.0)GO TO 78
      J0=1
   78 DO 86 J=1,J0
      WRITE(4)L0
      S0=0.0
      DR2=0.0
      DO 80 L=-5,4
      N=L0-6+L+J
      IF(N.LT.3)GO TO 80
      M=NE0+1-N
      X0=EIG(M)-2.0*EIG(M+1)+EIG(M+2)
      DR2=DR2+X0*TA0(L)
      S0=S0+TA0(L)
   80 CONTINUE
      DR2=DR2/S0  ;AVERAGED VALUE OF 2ND DIFF.
      IF(DR2.LT.-(0.32*DF0))DR2=-(0.32*DF0)  ;LIMIT NEG. DR2
      IF(DR2.GT.+(0.16*DF0))DR2=+(0.16*DF0)  ;LIMIT POS. DR2
      DR1=0.0
      S0=0.0
      DO 82 L=-5,5  ;SLIDING WINDOW SAMPLING
      N=L0-6+L+J
      IF(N.LT.2)GO TO 82
      M=NE0+1-N
      X0=EIG(M)-EIG(M+1)

      IF(X0.GT.(2.0*DF0))X0=(2.0*DF0)  ;THROW OUT LARGE DIFF.
      DR1=DR1+(X0-DR2*FLOAT(L))*TA0(L)
      S0=S0+TA0(L)  ;SUM OF TAPERS
   82 CONTINUE
      DR1=DR1/S0  ;AVERAGED VALUE OF 1ST DIFF.
C  COMPARE PREDICTED VALUE
      A0=0.0
      DO 84 L=-5,4
      N=L0-6+L+J
      IF(N.LT.1)GO TO 84
      M=NE0+1-N
      X0=FLOAT(L)
      A0=A0+EIG(M)-DR1*X0-(DR2/2.0)*(X0**2)
   84 CONTINUE
      A0=A0/FLOAT(L0-1)
      G0=A0+DR1*5.0+(DR2/2.0)*25.0  ;PREDICT L=5
      K=NE0+J-L0
      IF((EIG(K)-G0).GT.(2.0*DF0))I0=1  ;EIGENVALUE TEST FLAG
      WRITE(4,12)I0,DR2,DR1,A0,G0,EIG(K)
   86 CONTINUE  ;END OF J LOOP
      IF(I0.EQ.0)GO TO 88
      L0=L0-1  ;REDUCE L0
      I0=0    ;RESET I0
      GO TO 76
   88 NU0=NE0-L0-NU00  ;UNIQUE EIGENVALUES
```

2. ROOTFINDING ROUTINE

```
C     ROOT FINDING ROUTINE
  600 DO 602 N=1,NR0
      WTE(N)=CMPLX(999.999,999.999)
  602 CONTINUE
      N0=NR0  ;CURRENT ROOT INDEX
      IF(N0.EQ.1)GO TO 644
  610 Z=CMPLX(0.1,1.0)
      SFX(0)=CMPLX(1.0,0.0)
      SFX(1)=Z
      L0=0  ;ITERATION COUNTER INDEX
C  INSERT ESTIMATED ROOTS AT THIS POINT
      IF(KR0.EQ.0)GO TO 612
      IF(IQ9.GT.KDF)GO TO 612
      A0=PI0*SIN(PI0*DF0(IQ9)/180.0)
      X=COS(A0)
      Y=SIN(A0)
      Z=CMPLX(X,Y)
      SFX(1)=Z
      IQ9=IQ9+1
  612 CONTINUE
      I=0
      GO TO 620  ;INITIAL COMPUTE F(Z)
  614 I=1
      G0=F0
      M=0
      ALF=CMPLX(0.0,0.0)
      L0=L0+1  ;ADVANCE ITERATION COUNT
      DO 616 K=1,N0
      ALF=ALF+FLOAT(K)*CFE(K)*SFX(K-1)
  616 CONTINUE
      A0=CABS(ALF)**2
      DIF=-BET*CONJG(ALF)/A0
  618 M=M+1
      SFX(1)=Z+DIF
  620 CONTINUE
C  COMPUTE VALUE OF F(Z)
      A0=CABS(SFX(1))**2
      B=2.0*REAL(SFX(1))
      N2=N0-2
      DO 624 K=0,N2
      SFX(K+2)=B*SFX(K+1)-A0*SFX(K)
  624 CONTINUE
      BET=CMPLX(0.0,0.0)
      DO 626 K=0,N0
      BET=BET+CFE(K)*SFX(K)
  626 CONTINUE
      F0=CABS(BET)
      IF(F0.LT.TL1)GO TO 640  ;F(Z) NULL TEST
      IF(I.EQ.0)GO TO 614
      IF(F0.GE.G0)GO TO 630
      IF(CAB (DIF).LT.TL2)GO TO 640  ;ROOT TEST
      IF(L0.GT.IT0)GO TO 638
      Z=SFX(1)
      GO TO 614  ;NEXT ITERATION
  630 IF(M.GT.20)GO TO 632
      DIF=DIF/4.0
      GO TO 618
  632 LF1=1
      GO TO 640
  638 LF2=1
  640 CONTINUE
C  ROOT FOUND, STORE AND SUBTRACT IT OUT
      WTE(N0)=SFX(1)
      ALF=CFE(N0)
      CFE(N0)=CMPLX(0.0,0.0)
      Z=SFX(1)
      N1=N0-1
      DO 642 J=0,N1
      K=N1-J
      COP=CFE(K)  ;SAVE CFE(K)
      CFE(K)=ALF+Z*CFE(K+1)
      ALF=COP
  642 CONTINUE
      N0=N0-1  ;REDUCE N0 INDEX
      IF(N0.NE.1)GO TO 610  ;TEST FOR LAST ROOT
  644 BET=CFE(1)
      A0=CABS(BET)**2
      WTE(1)=-CFE(0)*CONJG(BET)/A0
      GO TO 250  ;ROOTS COMPLETED, RETURN TO IBN LOOP
```